WJE

I-40 Hernando deSoto Bridge

Fracture Investigation

Memphis, Tennessee

FINAL REPORT

October 7, 2021

WJE No. 2021.3178.1

PREPARED FOR:

Michael Baker International

PREPARED BY:

Wiss, Janney, Elstner Associates, Inc.
330 Pfingsten Road
Northbrook, Illinois 60062
847.272.7400 tel

I-40 Hernando deSoto Bridge

Fracture Investigation

Memphis, Tennessee

Brian J. Santosuosso
Principal and Project Manager

Jonathan C. McGormley
Principal

Robert W. Warke
Associate Principal

Timothy M. Kern
Associate III

FINAL REPORT
October 7, 2021
WJE No. 2021.3178.1

PREPARED FOR:
Michael Baker International

PREPARED BY:
Wiss, Janney, Elstner Associates, Inc.
330 Pfingsten Road
Northbrook, Illinois 60062
847.272.7400 tel

CONTENTS

INTRODUCTION

The 3.3-mile long I-40 Hernando deSoto Bridge crossing the Mississippi River was closed May 11, 2021 after inspectors performing a routine inspection identified a partial fracture in a tension member that supports one of two tied-arch truss spans. The fracture occurred at a welded plate transition in the upstream (north), box-shaped tension tie member (Figure 1). The six-lane bridge was subsequently closed to traffic.

The Tennessee Department of Transportation (TDOT) and the Arkansas Department of Transportation (ArDOT), joint owners of the bridge, assembled a team of consultants and a contractor to inspect and repair the bridge. Wiss, Janney, Elstner Associates, Inc. was retained to complete the forensic investigation of the fracture.

Figure 1. Annotated photo of partial tie girder fracture identified in May 2021 (photo courtesy of TDOT).

DESCRIPTION OF STRUCTURE

Opened to traffic in about 1973, the twin-span, tied-arch truss structure crosses the Mississippi River from Memphis, Tennessee to West Memphis, Arkansas with two continuous 900-foot long spans. This report focuses on the fracture that occurred within the tied arch span bridge unit. The span on the Arkansas side of the river is designated Span A while the span closer to Memphis is Span B. Within the bridge unit of interest, the superstructure is comprised of two, variable-depth trussed arches from which the reinforced concrete deck and its supporting structural steel framing is suspended via hanger cables. A box-shaped tie girder acts as a tension strut to restrain the outward thrust forces of the arches at the piers. The tie girders are bolted to the deck floor beams positioned below each hanger at 37 ft-6 in. centers. The hanger/floorbeam/tie girder connections are identified as T1 to T23 for both spans, numbered towards the shared center pier from each end (Figure 2).

The 32-inch deep by 26-inch wide boxed-shaped tie girder in each truss is continuous and consists of 1/2-inch thick top and bottom cover plates and two, 1 3/8-inch thick vertical side plates (Figure 3). To accommodate the net-section demands at the bolted hanger/floorbeam/tie girder connections, the thickness of the vertical plates is increased to 1 15/16-inches at odd numbered connections and to 2 1/4-inches at even numbered connections where the tie girder is spliced (Figure 4). The plate thickness transitions are formed through double-bevel groove welds (Figure 5).

For inspection purposes, each tie girder plate was numbered 1 to 8 depending on its location within the upstream (north) or downstream (south) tie. The weld locations were identified by span and by their locations east or west of the hanger. Refer to Figure 6 which provides the plate numbering identification system.

The cover plates and typical 1 3/8-inch thick side plates were fabricated from ASTM A514-69a Grade M steel plates while the thicker 1 15/16-inch and 2 1/4-inch thick side plates were fabricated from ASTM A517-69a Grade P PVA BAE material. Both materials had a specified minimum yield strength of 100 ksi. The grades M and P were both adopted in 1969. The 1970 specifications for the A517 material included requirements for Charpy V-notch testing.

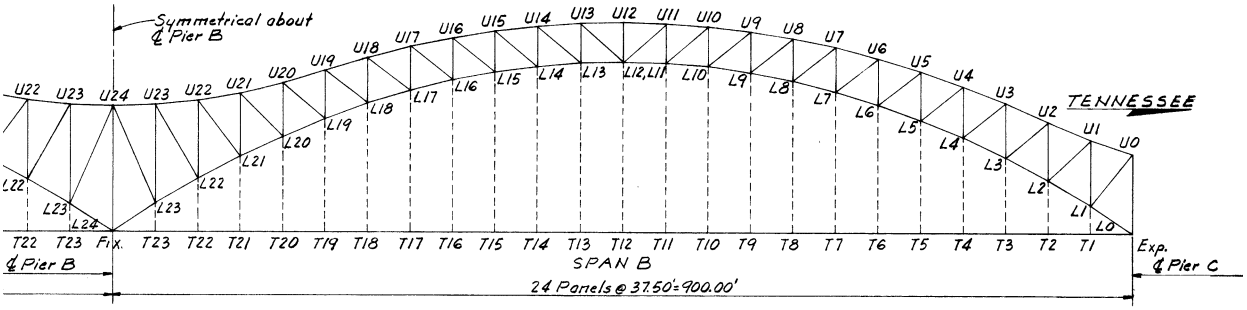

Figure 2. Arch Span B looking north with tie girder connection points labeled T1 to T23 from design drawings.

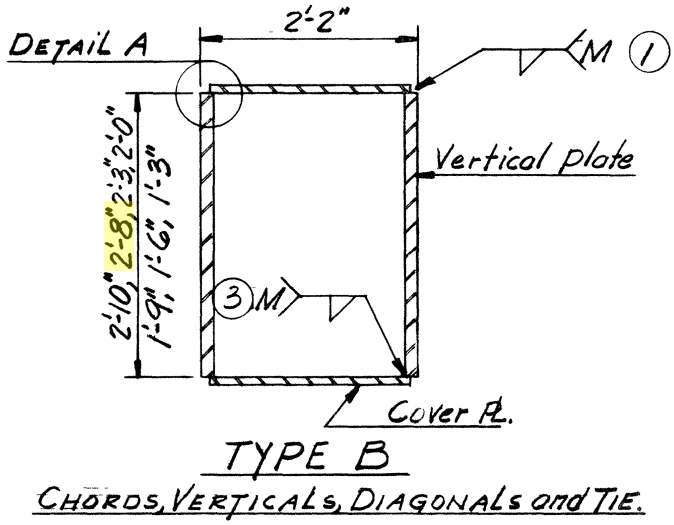

Figure 3. Type B bridge elements including tie girder section from design drawings (depth highlighted in yellow).

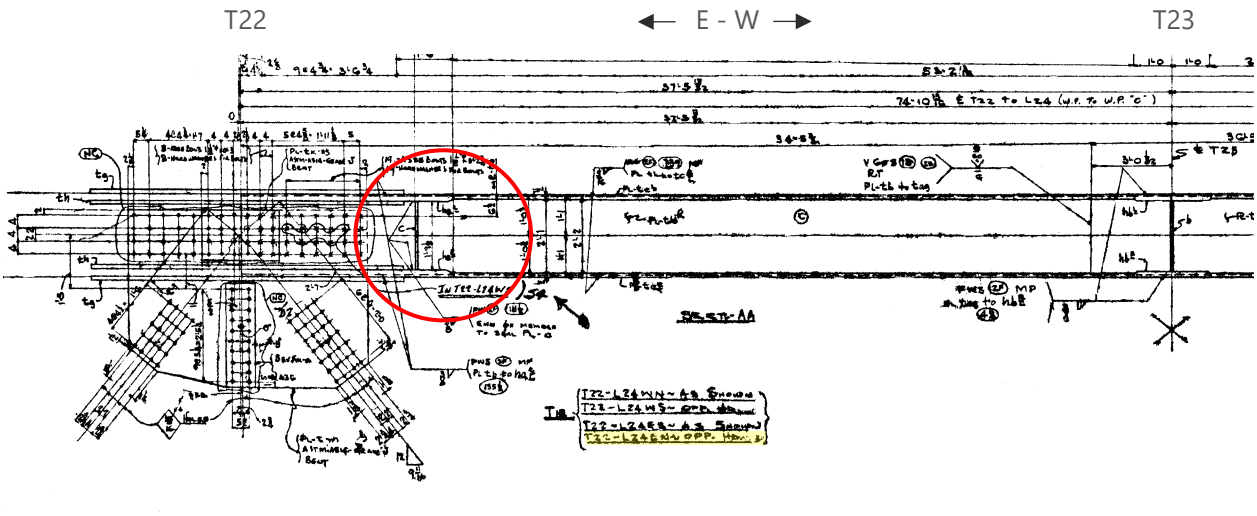

Figure 4. Shop drawing (longitudinal section view shown opposite hand) for tie at location of fracture (circled).

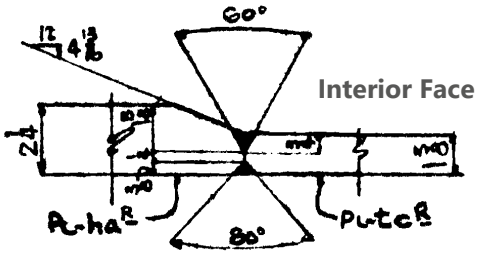

Figure 5. Side plate complete joint penetration groove weld details from shop drawings

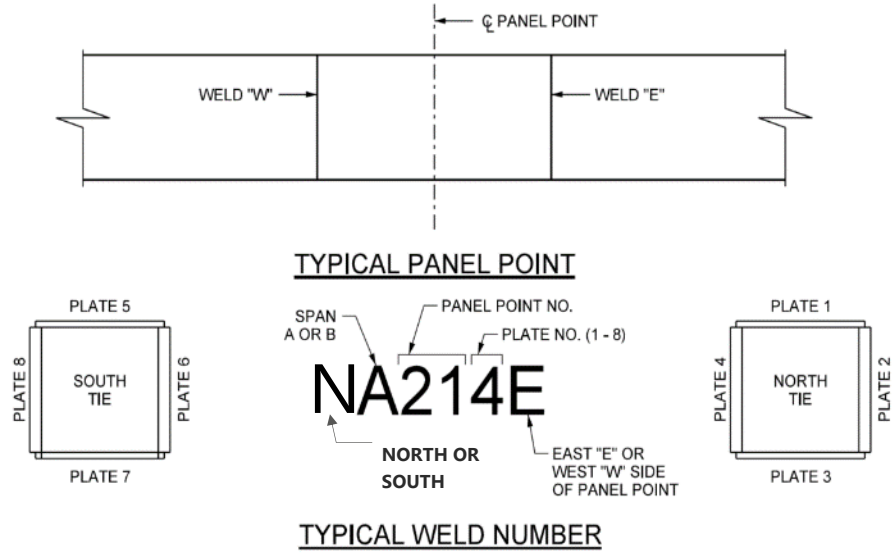

Figure 6. Identification of tie plates and welds (figure provided by HNTB).

BACKGROUND

The following information provides background relevant to the fracture and its propagation and most likely cause.

Fracture History

On May 11, 2021, while performing an inspection of the bridge hanger cables, bridge inspectors from Michael Baker International (MBI) observed a partial fracture of the tie girder just west of T22 at the welded splice in the north tie of Span B (NB222W). Figure 7 show views of the tie fracture. The bridge was subsequently closed to traffic.

A review of previous inspection records showed that a crack was present in the outboard side plate and likely the bottom cover plate in 2019 (Figure 8) and that it had extended between 2019 and 2021, fully fracturing the outboard side plate, top cover plate, and the longitudinal fillet weld connecting the top plate to the inboard side plate.

A photo taken by a kayaker in 2016 appears to show a crack-like indication from afar (Figure 9) at this same location.

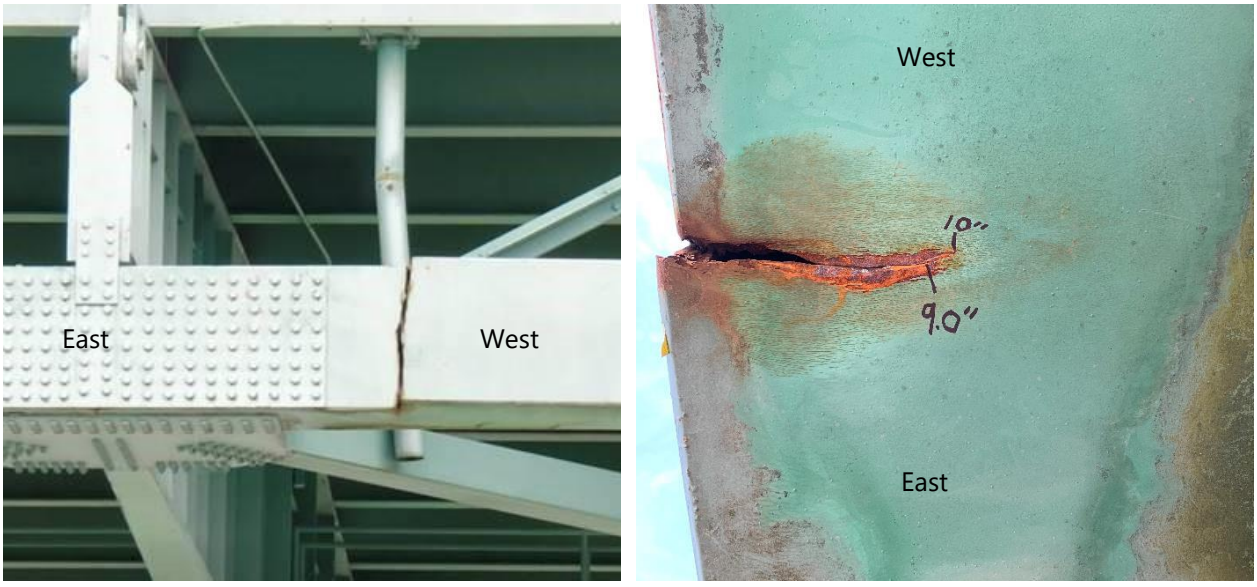

a. Fractured outboard tie plate (photo courtesy of TDOT). b. Partially fractured bottom cover plate.

Figure 7. Annotated photos of partial tie girder fracture identified in May 2021.

c. Cracked longitudinal fillet weld connecting top plate to inboard side plate (view looking west).

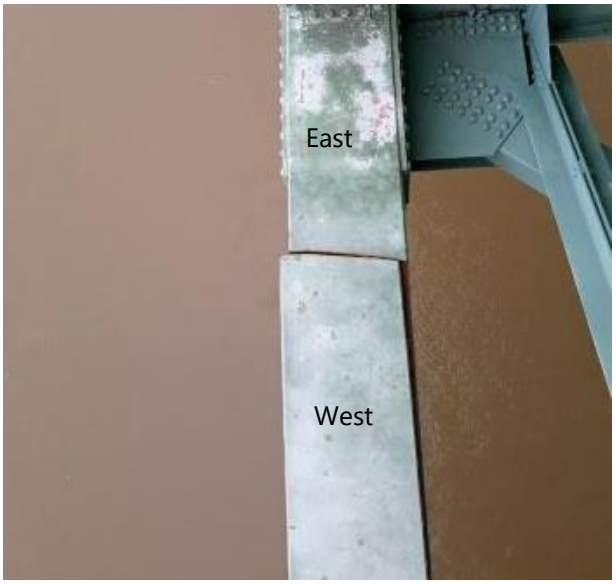

d. Fractured top cover plate (photo courtesy of TDOT).

Figure 7 cont. Partial tie girder fracture identified in May 2021.

Figure 8. An annotated screen-capture of the crack found by drone video footage from the May 2019 MBI inspection.

Figure 9. 2016 crack-like indication in tie girder (photo from Barry W. Moore via AP).

1982 UT Inspection

In 1982, an ultrasonic testing (UT) program was undertaken by TDOT to examine groove welds in the bridge. The reason for the inspection is not known nor is the scope of the project. Inspection records provided by HNTB show that a non-rejectable defect was found in the NB222W weld and recorded in the UT examination record (Figure 10). The defect was located 23 inches from the bottom of the side plate and 1 3/4 inches from the weld centerline. The one-inch long defect was characterized as slag.

After removal of the fractured pieces from the bridge, WJE was able to also identify this same defect using phased array ultrasonic test methods (PAUT). Subsequent sectioning of that location identified a shallow interior surface-breaking crack. The crack surface was opened as shown in Figure 11, revealing a 3/32-inch deep by 5/32-inch long crack.

MAGNAFLUX Quality Services

NDE EXAMINATION REPORT / AWS ULTRASONIC

FORM 22-2

INSPECTION SITE Hernando DeSoto I-40 Bridge Memphis, Tennessee CONTRACT NO. I-40-1(193)0, 79001-3144-44

ON Continuous Tied Arch Span B L24-T22 EN

FOR Tennessee Department of Transportation

Specification AWS D1.1-81 & AASHTO
Weld Joint Butt Weld
Weld Process Sub Arc Weld
Material A514
Material Thickness 2¼ to 1 3/8
Acceptance Standard PER AASHTO

Weld Identification NB222W
Equipment PS 710
Transducer Size .5X1.0 Angle 70°
Frequency 2.25
Couplant Cellulose

WELD GEOMETRY

PLAN VIEW

WELD LOCATION

Weld Identification	Extent of testing (Distance from "Y" of area tested if less than 100%)	Defect Number	Transducer Angle	Node	Decibels a Defect Level	b Reference Level	c Attenuation Factor	d Defect Rating	-X+ Defect Length	Angular Distance (Sound Path)	Depth From "A" Surface	Distance From "X"	Distance From "Y"	Defect Evaluation	Disposition (Accept or Reject)
NB222W	31½"	1	70°	1	15	25	1	+9	1"	1½"		+1 3/4"	23"	Slag	Accept

REMARKS One indication noted per this method within 5dB.

U.T. Operator & Lab Location	U.T. Interpretation By & Lab Location	Date
David Goforth L-II 6012		5-24-82

Figure 10. 1982 UT inspection record for Weld NB222W provided by HNTB.

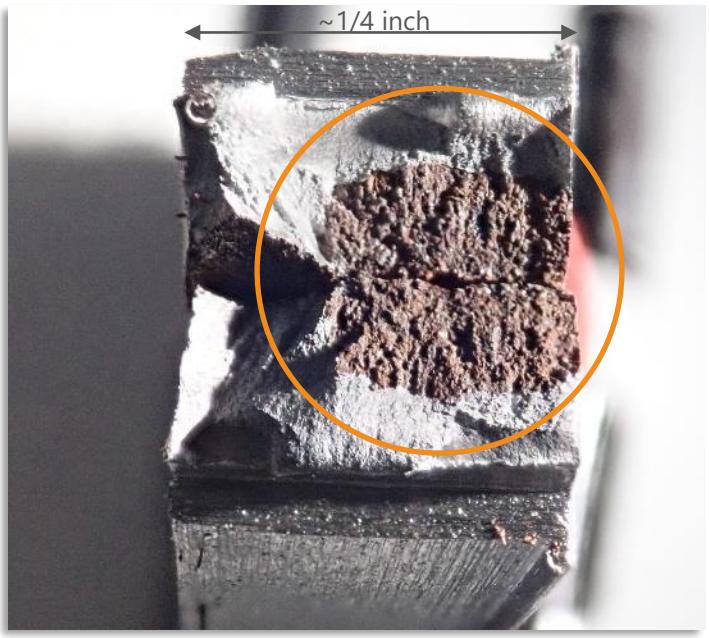

Figure 11. 1982-identified defect (circled) after crack surfaces revealed.

Tie Girder Thermal Behavior

As part of the repair operations, WJE was engaged to install instrumentation on the bridge to monitor the structure's behavior. Strain gages were installed on the upstream (north) and downstream (south) tie girders to monitor changes in load. Prior to installation of the permanent tie girders repairs, data were collected, a portion of which is presented in Figure 12.

The data show the south tie girder responds to changes in temperature much more significantly than the north tie girder. Both tie girders see an increase in load with decreasing temperatures with the decrease typically occurring in the early morning hours. These data were collected in May when the sun was approaching its northern-most position. Direct exposure to sun tended to reduce the tie tensions.

For this structure, the total design dead load in each tie girder was 4,575 kips. The design live load increased the tension in the ties by only 890 kips or about 16 percent. The thermal data shows a nearly 300 kip increase in tie girder load with a 20 deg. F drop in temperature or nearly a third of the maximum live load plus impact demand. The upstream tie girder experienced about a 160 kip increase in tie tension with the same drop in temperature. It was reported as part of a previous thermal study of the bridge[1] that the Pier A pendulum bearings overcame friction at an estimated load of 250 kips while the Pier C bearings moved at a load of 212 kips. Thus, it was postulated that the pendulum bearing slip load would serve to limit the maximum thermal force that could be realized in the tie girders. However, the data used to develop these slip limits were limited. Moreover, the data shown in Figure 12 do not indicate that slip of the bearings occurred.

[1] Bravo Alexander, J. R., "Structural Health Monitoring of the Hernando deSoto Bridge", May 2017, ProQuest LLC 10262356 (2017), Ann Arbor, MI

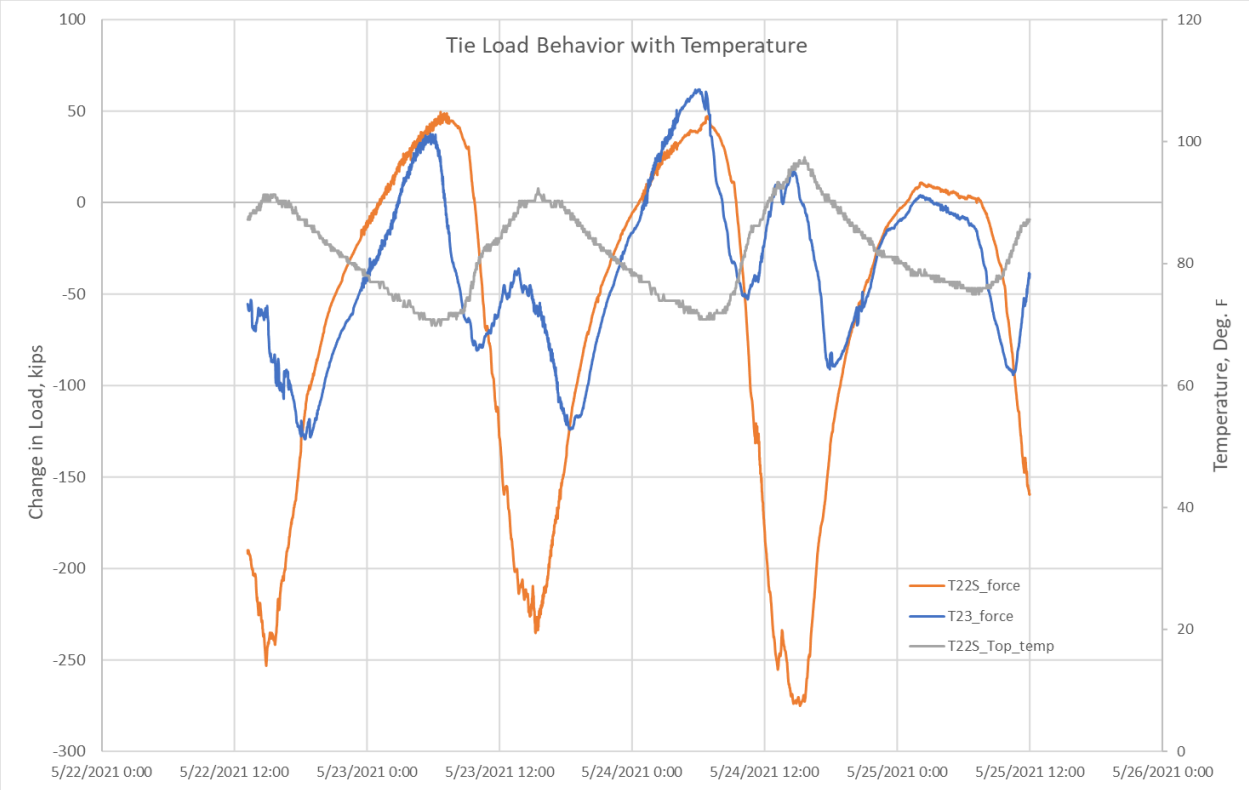

Figure 12. Change in load of north (blue) and south (orange) tie girders with changes in temperature (grey).

Temperature History

Temperature records for Memphis over the last fifty years were reviewed. Figure 13 provides a list of annual low temperature events over that time period. These data were collected at the Memphis International Airport. Since 2019, the lowest temperature has been 9 deg. F on February 15, 2021. Since the bridge was constructed there have been twenty minimum low temperatures of 10 deg. F or below with the coldest temperatures of -4 deg. F recorded in 1985 and 1989.

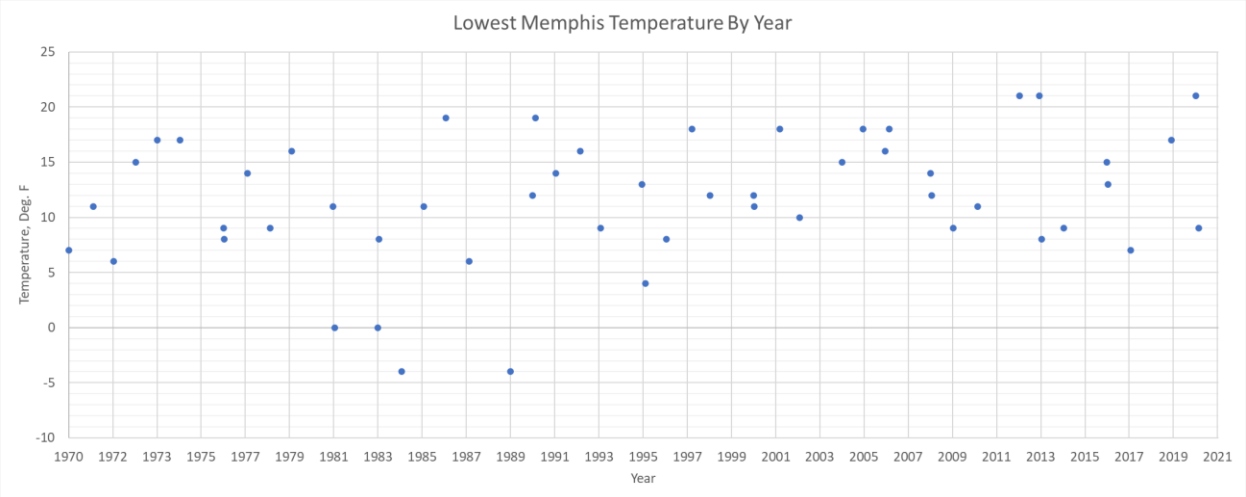

Figure 13. Annual lowest temperatures in Memphis.

Sample Removal

Following the installation of a jacking system to temporarily support a portion of the north tie girder load, the fractured portions of the top and bottom cover plates and outboard (north) side plate were removed from the bridge by Kiewit Infrastructure South Co. and transported to WJE's Northbrook, Illinois laboratory for examination and evaluation. A combination of plasma and oxygen-acetylene torch cutting were used to remove the pieces of plate from the bridge (Figure 14).

In addition to the fractured plates, ten 3-inch diameter core samples were removed by WJE at locations identified by PAUT has having possible defects. A core sample extracted from the weld at SA168W is shown in Figure 15. The ten core locations are shown in Figure 16.

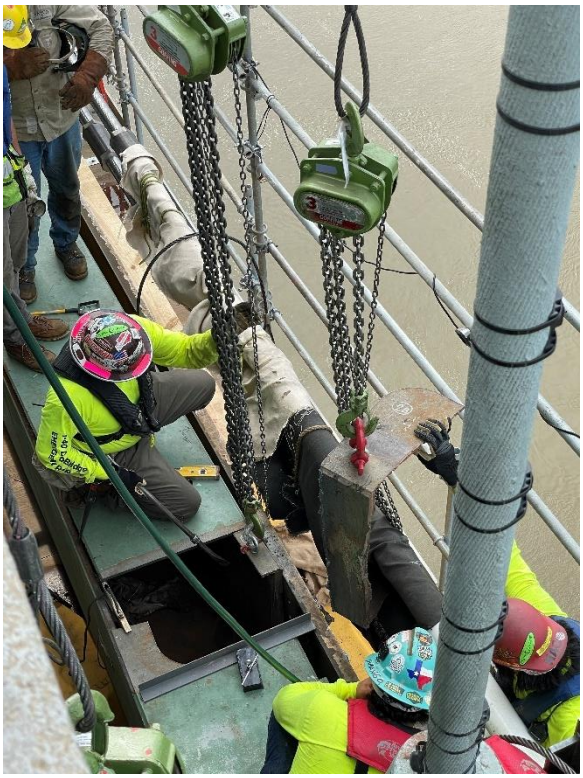

Figure 14. Removal of fractured pieces from tie.

Figure 15. View from inside tie showing core sample removed from groove weld.

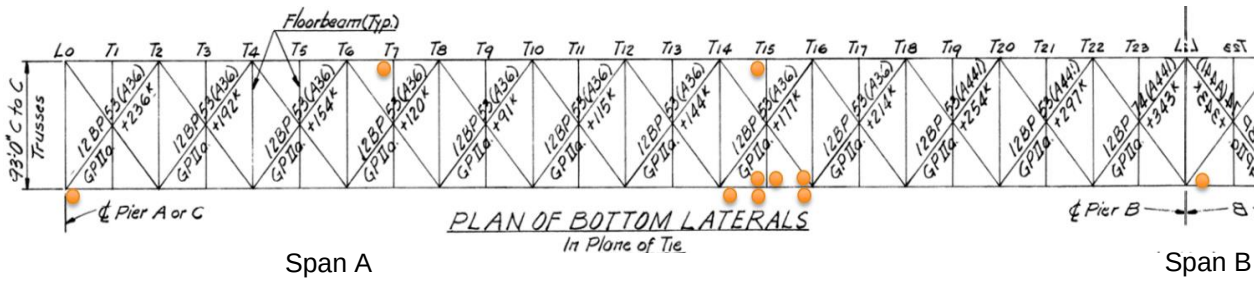

Figure 16. Locations in Span A of core samples removed from other tie girder groove welds with defect indications.

MATERIALS STUDIES

A section of the fractured north tie girder just west of T22 in Span B was removed from the bridge and sent to WJE's laboratory in Northbrook, Illinois for metallurgical evaluation. Fractographic and metallographic examinations were carried out to determine the cause of failure and any contributing factors. Additionally, the material was tested to determine if the steel conformed to the relevant requirements of ASTM A514 *Standard Specification High-Yield-Strength, Quenched and Tempered Alloy Steel Plate* and ASTM A517 *High-Strength Alloy Steel Plates, Quenched and Tempered, for Pressure Vessels*, as specified in the shop drawings documents. The following presents the findings from our materials studies.

Optical and Scanning Electron Fractography

Figure 17 shows the two as-received east and west mating fracture surfaces from location NB222W. The photograph was taken prior to any cleaning or sectioning. Most of the fracture had occurred near the fusion line between the weld metal and the thinner 1 3/8-inch side plate on the west side of the fracture.

The east sample was used for mechanical testing, metallurgical analysis, and ultrasonic inspection while the west sample was used for mechanical testing with limited metallurgical analysis. Figure 18 denotes the cut lines where the material was sectioned for further analysis from the east sample. The west fracture was not utilized for the primary fractographic and metallographic analysis because portions of the fracture surface had been inadvertently sandblasted in preparation for removal of the fracture pieces. The discoloration along portions of the fracture surface indicative of sandblasting is shown in Figure 19.

Two regions in the samples exhibited markedly different macrotopography from the rest of the main fracture surfaces and are noted in Figure 20 and Figure 21 as Primary Preexisting Crack and Secondary Preexisting Crack. The former had a maximum depth of about 1 1/16 inch and a length of 6 3/4-inches. The latter extended nearly 1 5/16-inch through the 1 3/8-inch thickness of the side plate with a length of 8 inches. After ultrasonic cleaning in a solution of Alconox in water at ~100 deg. F for about one hour, enough rust had been removed from the east fracture face to discern essentially all of its macrotopography. Radial lines and chevron patterns emanating from both regions indicated that the region closest to the bottom plate, shown as View A in Figure 21, was the overall fracture origin and therefore the primary preexisting crack.

The initial unstable fracture (❶) that propagated out of the primary preexisting crack extended in all possible directions: through a portion of the remaining plate thickness toward the side plate's exterior surface; downward toward the bottom plate, where it arrested at the bottom plate fillet welds; and upward toward the top plate, where it was arrested by the secondary preexisting crack (Figure 21, View B). In the through-thickness direction, the initial fracture was arrested before it reached the external (outboard) surface of the side plate, leaving an intact ligament ~3/16 thick (Figure 21). In the upward direction, the arrest of the initial fracture within the secondary preexisting crack apparently did not rupture the ~1/8-inch-thick ligament that remained between the outer tip of the secondary preexisting crack and the exterior (outboard) surface of the side plate (Figure 21).

The upper tip of the upper, secondary preexisting crack exhibited a second fracture initiation site (Figure 21), from which a fracture (❷) extended upward for approximately 8 inches, then rearrested in the 1 3/8-inch plate material. This transient fracture event appears to have caused the tensile-shear rupture of

the side plate's remaining exterior-side ligament, thus making the crack visible to external observation. This event also caused the lower tip of the initial fracture to extend about 7 inches into the bottom plate as a tensile-shear fracture. The tensile-shear failure in the bottom cover plate is consistent with the observed paint yielding around the crack.

A third fracture initiation (❸) resulted in yet another fracture that separated the remaining 6 1/2 inches of the side plate's height and continued into the top cover plate (Figure 22). Careful examination of the entire length and width of the preexisting cracks and fracture surfaces associated with NB222W produced no evidence of fatigue crack growth.

A summary of the fracture propagation through the tie girder cross section is shown in Figure 23. The yellow and green represent the initial preexisting cracks. The colors blue (❶), orange (❷), and magenta (❸) represent the first, second, and third unstable fracture growth, respectively.

Examination of the fracture surfaces by scanning electron microscopy (SEM) began with the secondary (upper) preexisting crack on the east fracture face since it had been less corroded than the primary (lower) preexisting crack. Although the entire surface was found to be somewhat damaged by sandblast overspray and corrosion, a careful survey of the secondary preexisting crack region like that shown in Figure 24 identified several locations consistent with the microtopography produced by transgranular hydrogen cracking (Figure 25). Weld-related hydrogen cracking may be intergranular or transgranular, depending on the microstructure, hydrogen concentration, and state of stress.

The surface of the primary (lower) preexisting crack (Figure 26) was found to be more extensively damaged by post-failure corrosion, as typified by the pitted microtopography shown in Figure 27. However, a careful search provided fractographic clues at two separate locations within the area shown in Figure 28, just beneath the inside surface of the side plate. As interpreted within the context of the overall macrotopography, the microtopography at these locations indicated plateaus of intergranular hydrogen cracking in columnar-grained weld metal, connected to each other by ductile tearing (Figure 29 and Figure 30).

A core sample was taken from the arrested crack tip in the bottom cover plate in preparation to remove the two fracture surfaces from the tie girder. Photographs of the core sample are shown in Figure 31 and Figure 32. A small pie wedge shape was removed from the core and broken open to observe the crack tip at higher magnifications, which revealed shear fracture driven by tension. The exposed crack tip is shown in Figure 33. No evidence of fatigue was observed. Figure 34 depicts a prior arrest mark on the exposed surface.

Figure 17. As-received sample from the fracture at NB222W for laboratory analysis.

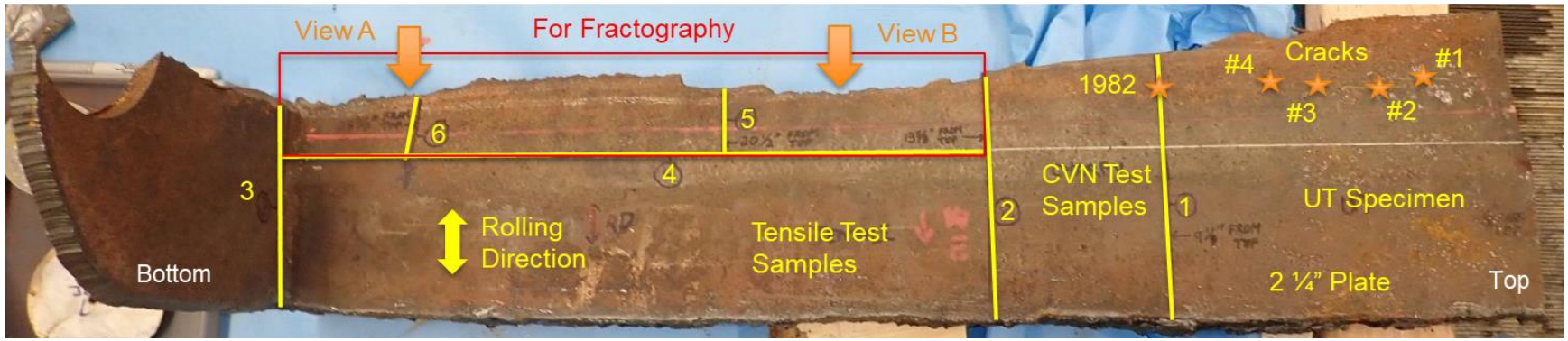

Figure 18. Overall photograph of the east fracture surface depicting the samples used for mechanical testing and metallographic analysis prior to sectioning.

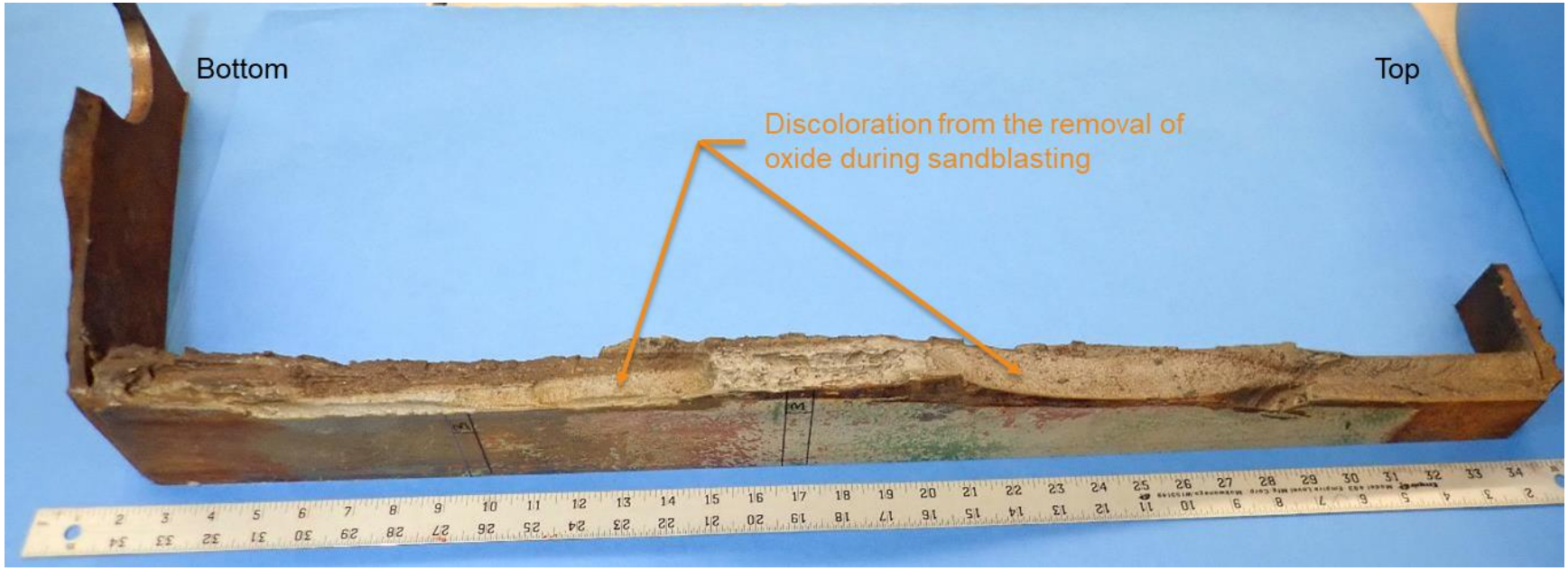

Figure 19. West fracture surface (left piece shown in Figure 17).

Figure 20. Lower portion of fracture showing Primary Preexisting Crack Region (yellow) and the Secondary Preexisting Crack Region (green).

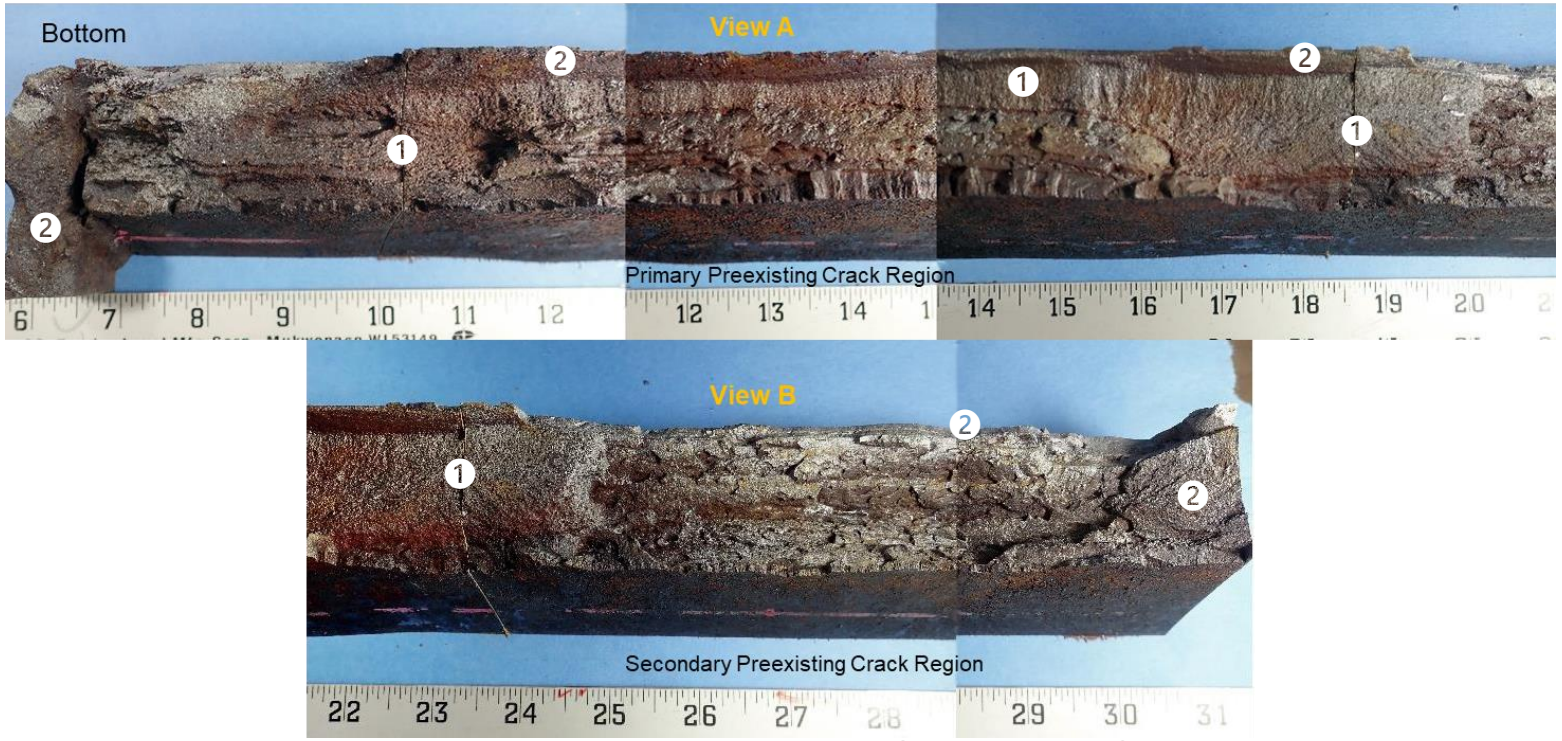

Figure 21. Higher magnification of the two preexisting crack regions after cleaning (❶ first fracture and ❷ second fracture).

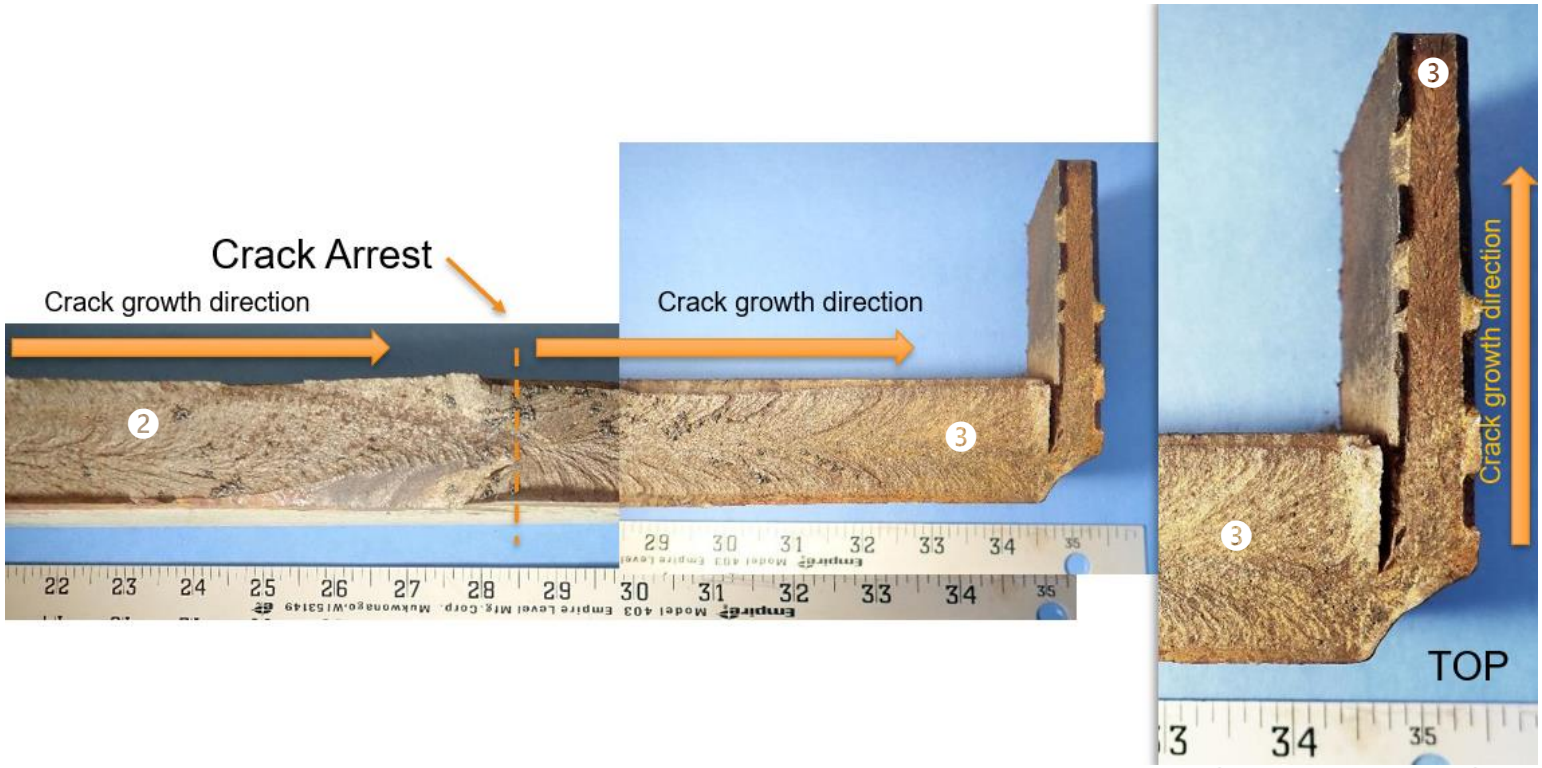

Figure 22. Top section of the crack in the west fracture. The orange arrows indicate the direction of crack growth (❷ second fracture and ❸ third fracture).

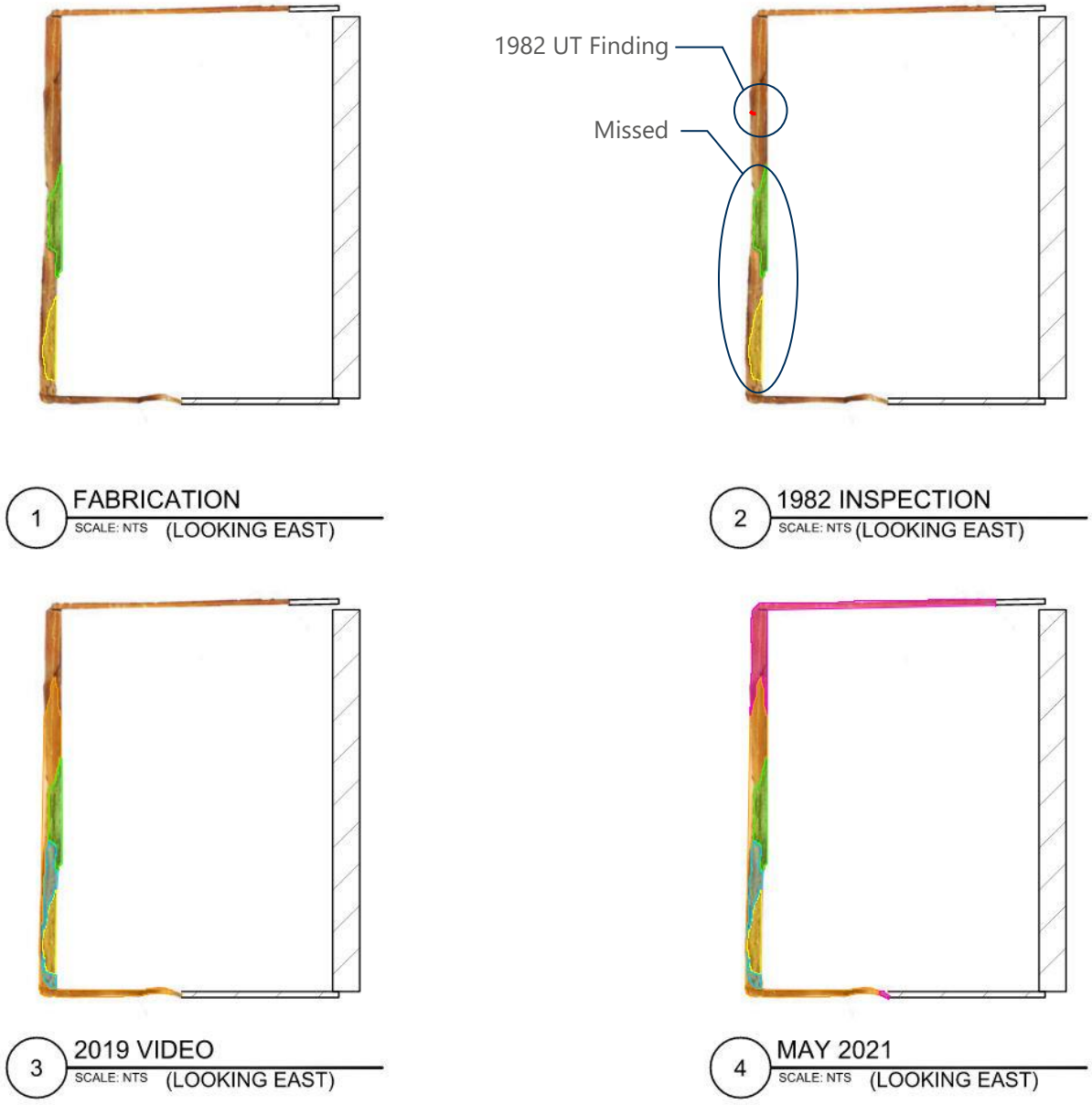

Figure 23. Postulated progression of fracture through tie girder cross section. Initial hydrogen cracks (yellow and green). First fracture (blue). Second fracture (orange). Third fracture (magenta).

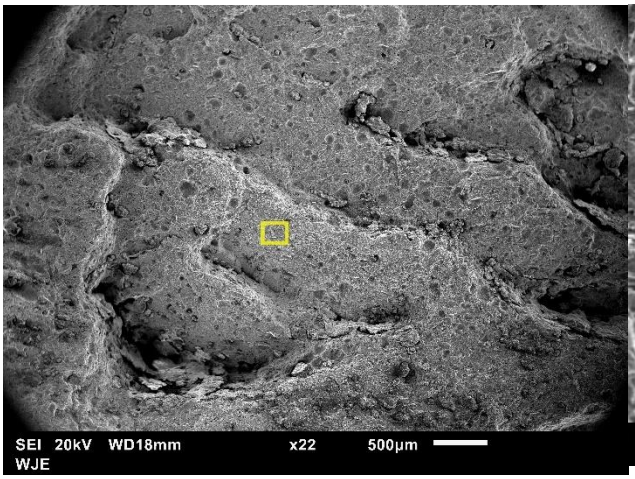

Figure 24 Low-magnification (22X) SEM image of secondary preexisting crack.

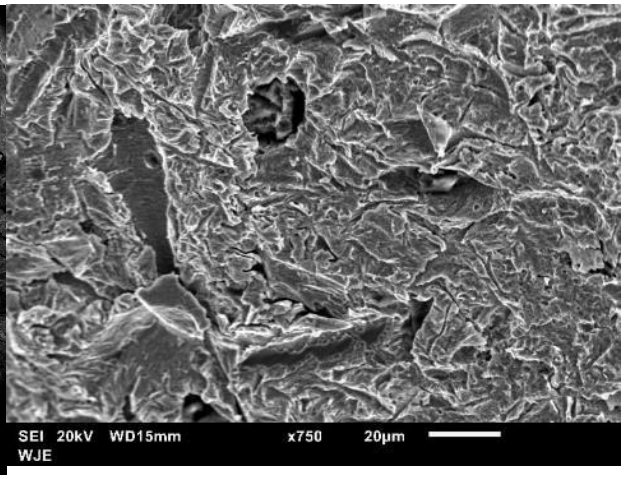

Figure 25. More highly magnified (750X) SEM image obtained from region inside box shown in Figure 24.

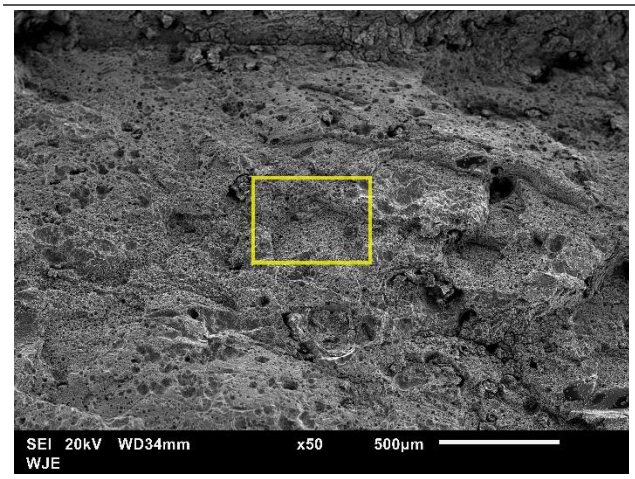

Figure 26. Low-magnification (50X) SEM image of primary preexisting crack.

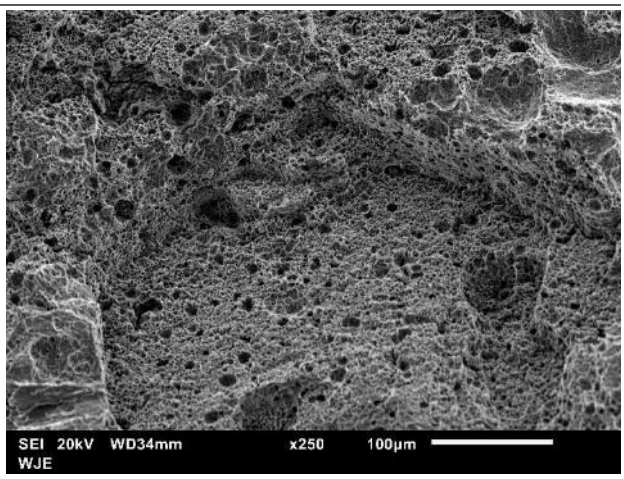

Figure 27. More highly magnified (250X) SEM image obtained from region inside box shown in Figure 26.

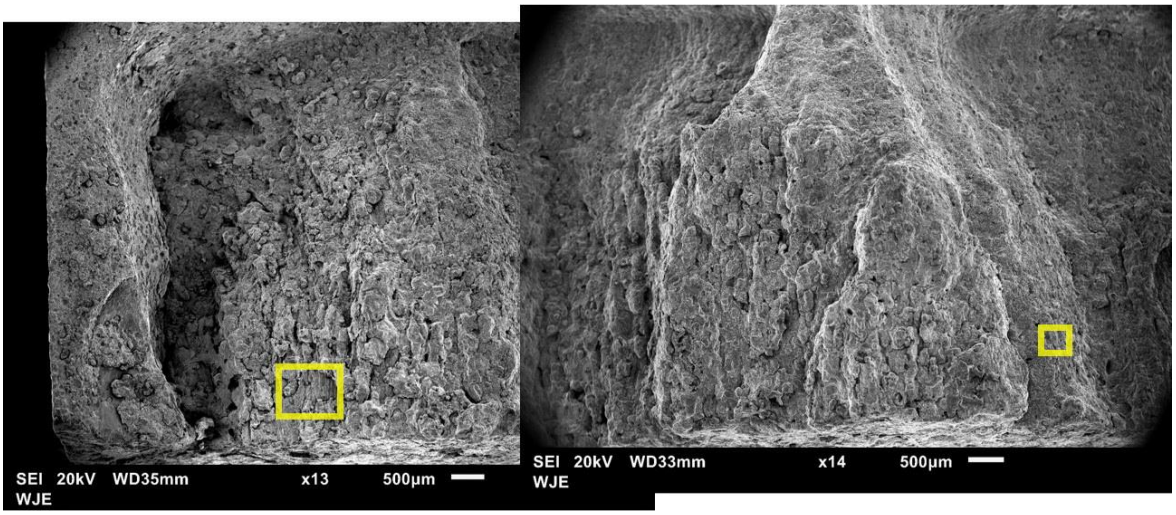

Figure 28. Low-magnification (13X and 14X) SEM images of primary preexisting crack. Internal surface of side plate is visible along bottom.

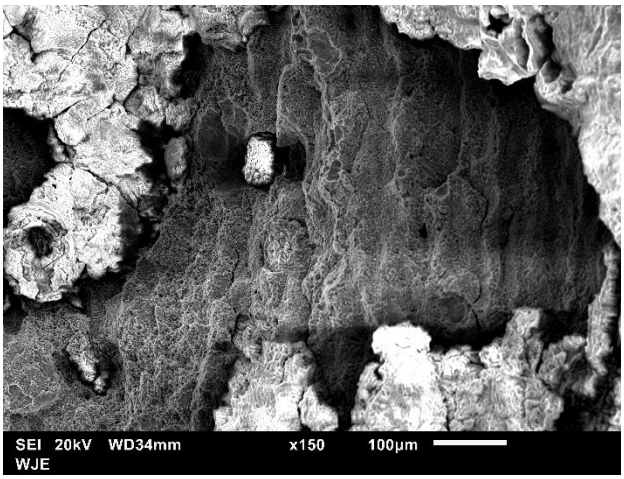

Figure 29. More highly magnified (150X) SEM image obtained left box within Figure 28

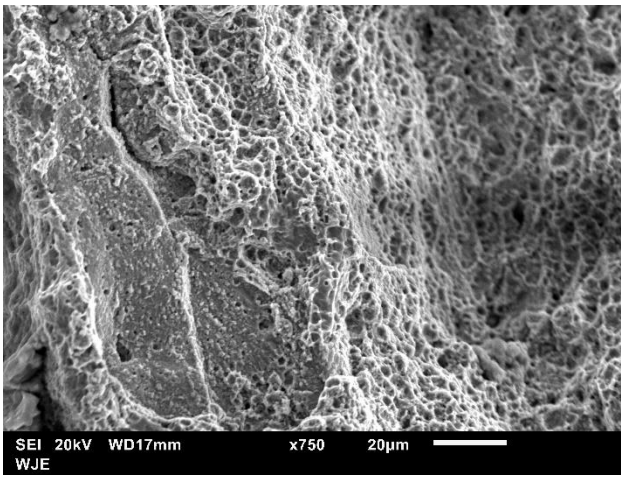

Figure 30. More highly magnified (750X SEM image obtained from right box within Figure 28.

Figure 31. Core in the bottom flange plate at the arrested crack tip.

Figure 32. Sectioned core from the arrested crack tip.

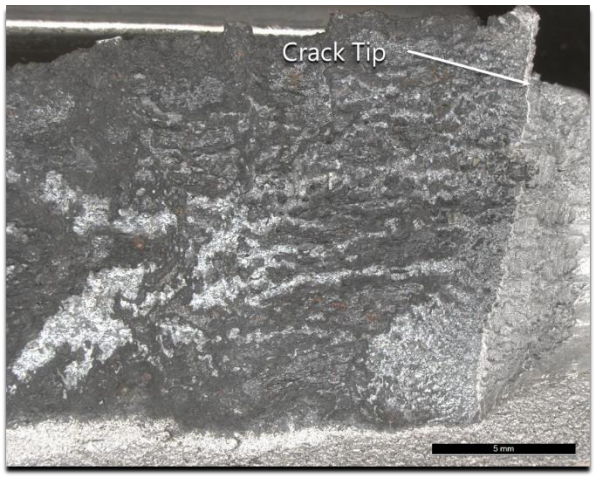

Figure 33. Arrested crack tip fracture surface.

Figure 34. Previous arrest mark (arrow away from the crack tip).

Optical Metallography and Microhardness Testing

Samples for metallographic assessment were prepared in WJE's metallographic laboratory using an assortment of specialized tools. A combination of wet and dry metallurgical saws was used to section the samples and to prevent any deformation, contamination, or heating of the surfaces prior to assessment. After sectioning, the smaller samples (<1.25-inch largest cross-sectional diameter) were mounted in a thermosetting polymer compound. Larger samples were mounted in a slow-cure epoxy resin. Samples were then "rough" ground using a progressively finer set of wet silicon carbide sanding discs on a polishing wheel down to a final grit of 1200. After "rough" grinding, the samples were polished using diamond-embedded cloths down to a final surface finish of 0.05 micron. Samples were then etched using a 2% nital (2% concentrated nitric acid, 98% methanol) to enhance the surface topography of the samples and reveal the microstructure of the steel when viewed under an optical microscope.

Four large-format cold mount samples were removed from the mating surfaces of the fracture at locations indicated by the orange arrows shown in Figure 35. A low magnification montage was assembled as Figure 36 to examine the full cross-section of the primary preexisting crack. The 2 1/4-inch plate is on the left side of the weld and the 1 3/8-inch plate is on the right. The crack was observed to pass through the weld metal, heat affected zones (HAZ), and base metal. Figure 37 displays a montage of the two mating surface samples prepared at the secondary (upper) preexisting crack region of the weld. In this section, most of the crack growth progressed through weld metal.

Coarse grains were observed in the base metal of the 2 1/4-inch plate adjacent to the weld fracture. ASTM-A517-69a requires a grain size of 5 or finer for this material. Figure 38a highlights an area in the 2 1/4-inch base metal viewed at a magnification of 100X with a grain size comparator overlayed. The austenite grains are coarser than an ASTM grain size of 1. Using the core samples removed from other welds in the bridge as comparators, samples of the 2 1/4-inch plate were examined and found to have average grain sizes much finer and meeting the ASTM specifications. Micrographs of three core samples are shown in Figure 38b-d.

Microhardness readings were taken using a Knoop indenter and a 500-gram load in accordance with ASTM E18–17. The readings were taken from the mating surface samples of both the upper and lower preexisting crack regions. The hardness values are presented in Table 1 and are identified by the microstructure at the test location. A hardness reading was performed in the HAZ and the weld metal at seven different elevations on each side of the fracture. ASTM A514-69a (applicable to the 1 3/8-inch plate) specifies a hardness between 235 and 293 Brinell (99 Hardness Rockwell B (HRB) to 31 Hardness Rockwell C (HRC) or 247 Hardness Vickers (HV) to 309 HV) when tensile testing is not performed. No hardness requirements are defined by ASTM A517-69a for the 2 1/4-inch material.

The grain-coarsened heat-affected zone (GCHAZ) hardness was significantly higher than the specified base plate material hardness. The maximum recorded hardness in the GCHAZ was 371 HV (38 HRC) in the primary preexisting crack region and 414 HV (42 HRC) in the secondary preexisting crack region.

When the two montages of the weld profiles cut from the preexisting crack regions (Figure 36 and Figure 37) were viewed in comparison to the weld region near the top of the fractured side plate or with welds contained in the core samples, the weld profiles from the preexisting crack regions were significantly wider. Figure 39 and Figure 40 show these comparisons. Moreover, the placement of the weld beads differed in that welds shown in Figure 39b and Figure 40a and b indicated the inside bevel weld had been placed first with the two plates laid flat, as shown in the photo, followed by the second bevel weld after the plates were flipped over. In comparison, the welds in the preexisting crack regions showed the inside weld beads having been placed after the outside weld, and the weld bead stacking arrangement appeared to have been misaligned with the root of the weld. This suggested that the two preexisting crack regions were likely weld repairs.

Table 1. Microhardness readings at preexisting crack regions.

Primary (Lower) Preexisting Crack				Secondary (Upper) Preexisting Crack			
Weld Metal		GCHAZ		Weld Metal		GCHAZ	
HRC	HV	HRC	HV	HRC	HV	HRC	HV
32.0	318	35.0	346	34.0	333	42.0	414
32.0	322	34.0	333	26.0	273	28.0	289
32.0	317	32.0	322	25.0	270	30.0	303
30.0	301	32.0	317	28.0	290	28.0	290
33.0	323	38.0	371	38.0	373	42.0	408
30.0	302	32.0	322	36.0	350	35.0	347
34.0	334	38.0	371	31.0	309	33.0	325

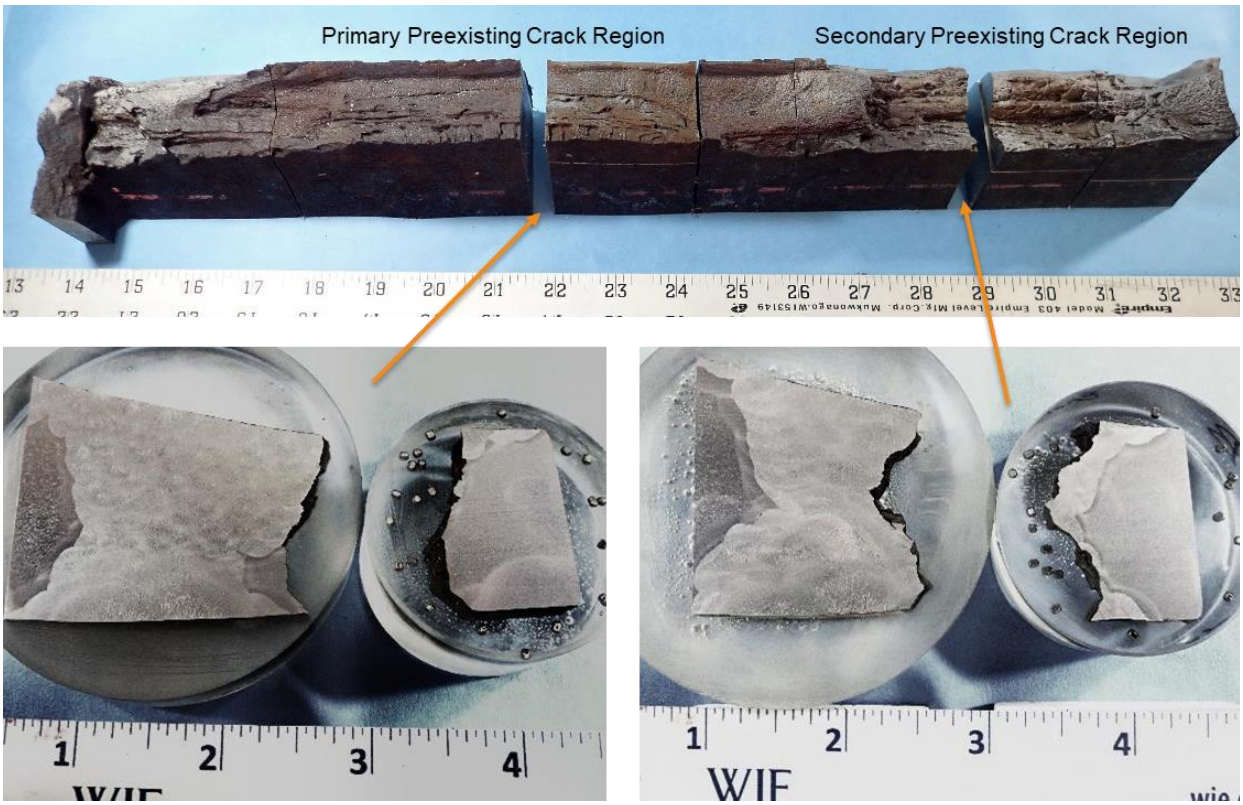

Figure 35. Overall primary and secondary preexisting crack regions along the fracture surface and associated mating fracture surface prepared for metallographic examination.

Figure 36. Primary (lower) preexisting crack region shown in a low-magnification montage.

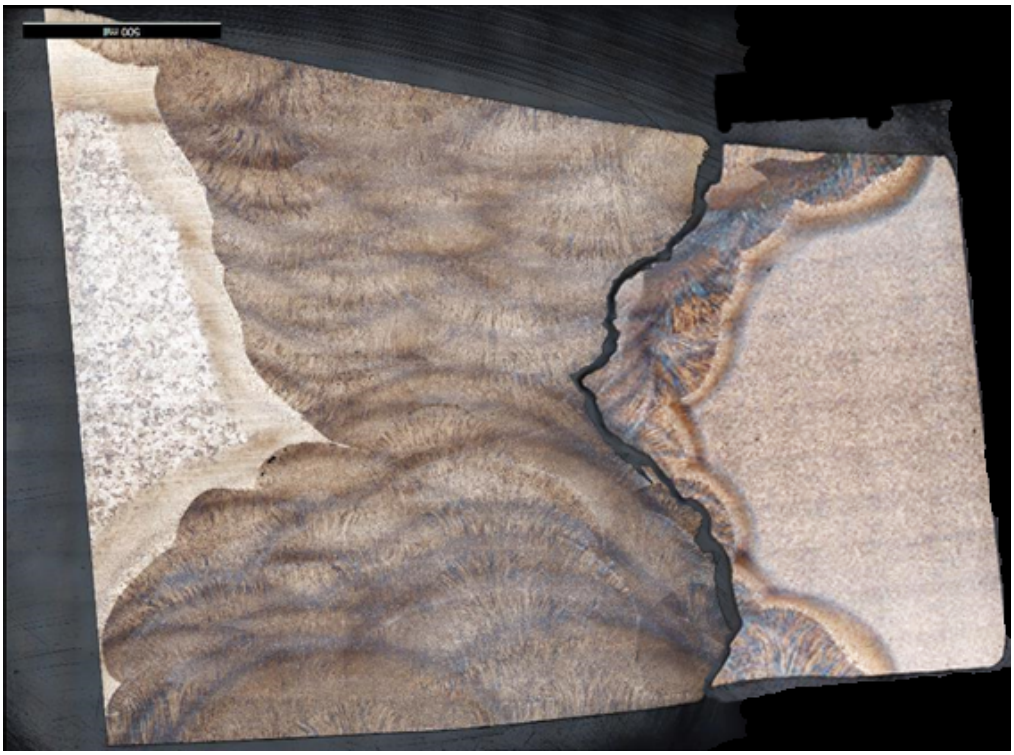

Figure 37. Secondary (upper) preexisting crack region shown in a low-magnification montage.

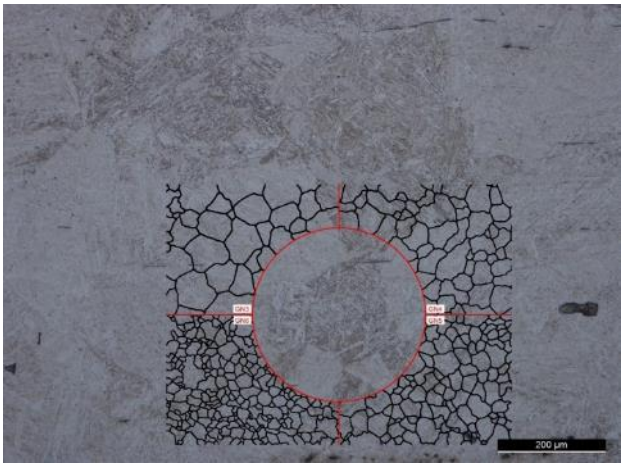

a. Large grain size in fractured plate.

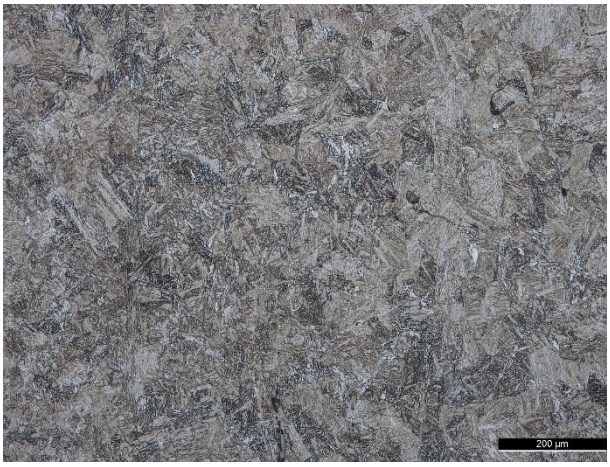

b. Core Sample SA008E.

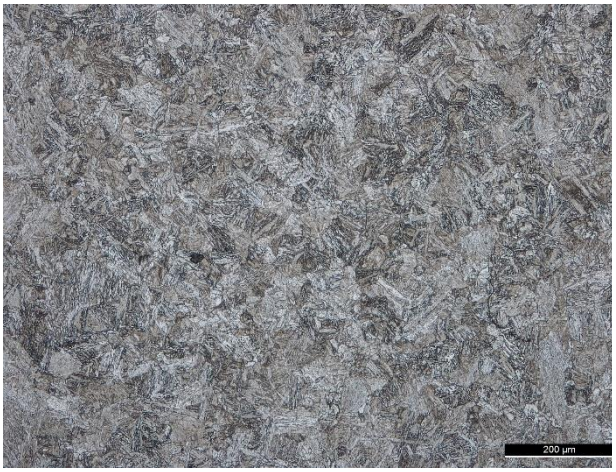

c. Core Sample SA148E.

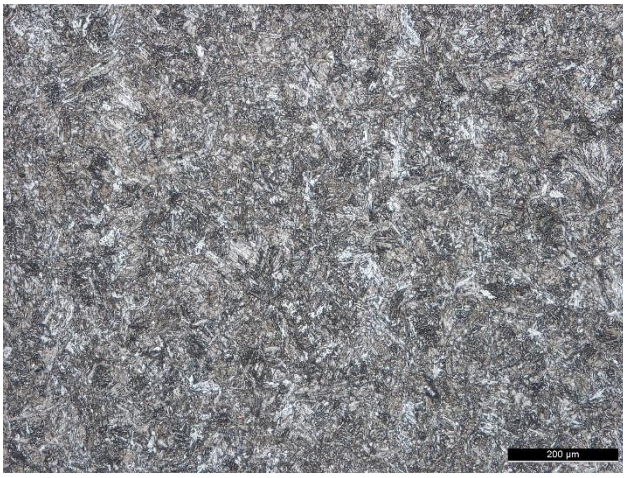

d. Core Sample SB246E.

Figure 38. Comparison of grain sizes for 2 1/4-inch plate – 100X magnification.

a. Primary Preexisting Crack weld profile.

b. Weld profile near top of fractured side plate.

Figure 39. Comparative weld profiles in fractured side plate.

a. Core Sample SA008E weld profile.

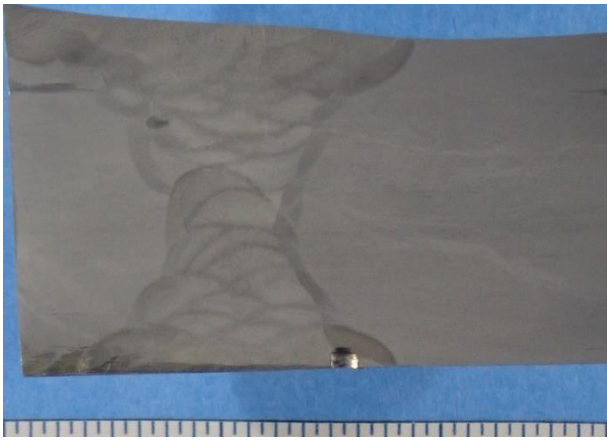

b. Core Sample NA154W weld profile.

Figure 40. Comparative weld profiles from representative core samples.

Optical Metallography and Microhardness Testing of Other Cracks Along Fracture

A previously identified flaw in the vicinity of the fracture is shown in Figure 41a. Optical and SEM fractography were performed to evaluate its characteristics. The crack was opened to view the fracture surface (Figure 41b). Surface oxides were present on the fracture surface, which exhibited a typical thumbnail shape. This fracture was further examined in the SEM at magnifications of 25X (Figure 41c) and 250X (Figure 41d). Figure 41d indicates that the fracture mode of the crack was intergranular.

In addition to the 1982 detected flaw, another indication was identified using PAUT by WJE and exposed for metallography. This defect was identified as Indication #4. A montage of this sample is shown in Figure 42. The crack initiated in the weld metal on the bottom surface (relative to the micrograph) and progressed halfway through the sample. Figure 43 provides a closer perspective of the crack tip at 50X magnification. The cracking was predominantly intergranular with limited transgranular cracking. The microstructure of the weld metal is presented at 500X magnification in Figure 44. It is predominantly martensite.

Microhardness readings were taken at Indication #4. Both a vertical and horizontal hardness traverse were performed near the crack. The results are presented in Figure 42. The results exhibited consistent hardness measurements between 360 HV and 385 HV (36.9 HRC to 39.5 HRC).

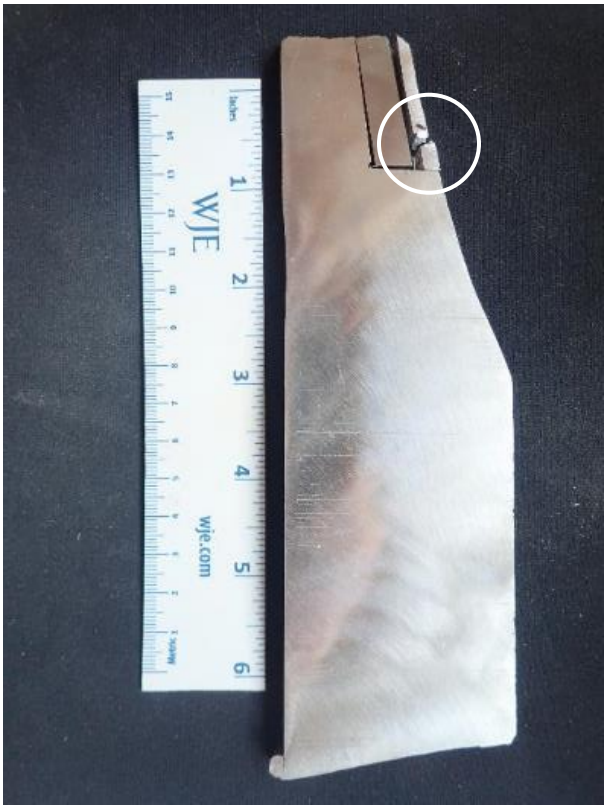

a. Sample cut from fracture piece.

b. Fracture surface of the flaw (circled region from a).

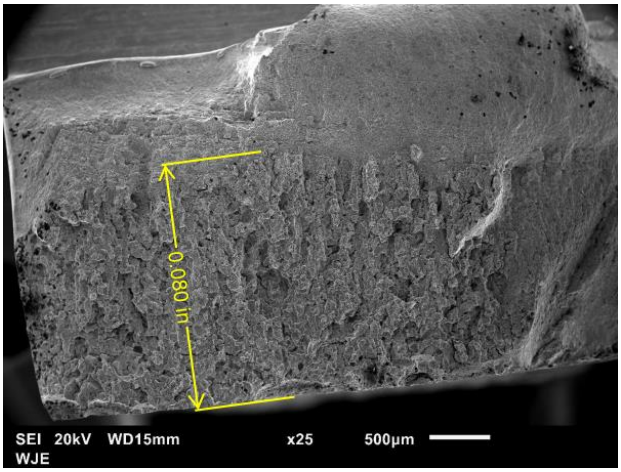

c. SEM micrograph of crack at 25X magnification.

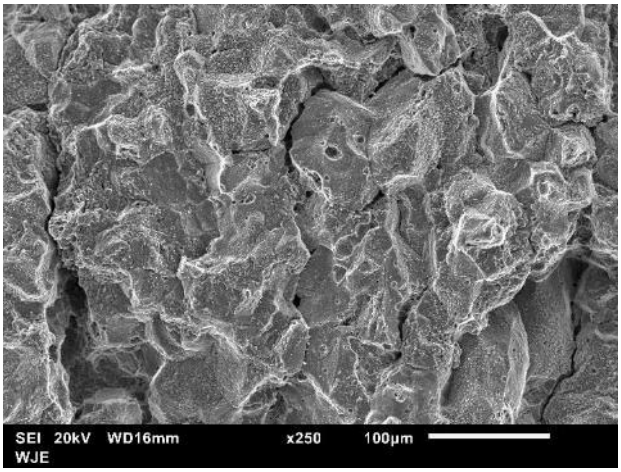

d. SEM micrograph of crack at 250X magnification.

Figure 41. 1982 previously identified crack near fracture.

Defect Indication #4 (all weld metal)	Location	HRC	HV
Vertical traverse	From inside surface moving downward	39.3	383
(approximately 0.010 in spacing)		37.6	367
		37.3	364
		39.5	385
		37.0	361
Horizontal traverse	From left to right	36.9	360
(approximately 0.010 in spacing)		37.2	363
	Left of crack	37.3	364
	Right of crack	37.4	365
		37.5	366
		37.0	362

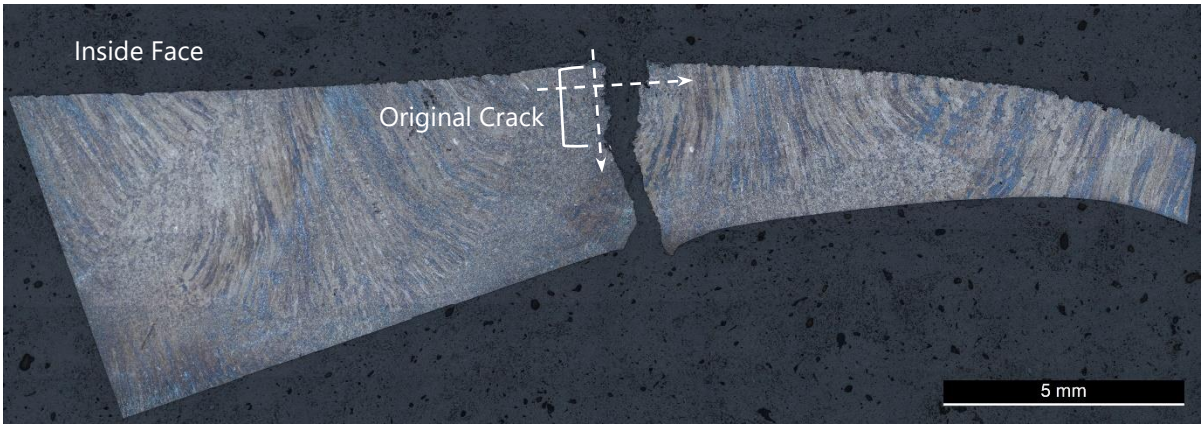

Figure 42. Microhardness traverse locations (dashed lines)for defect Indication #4.

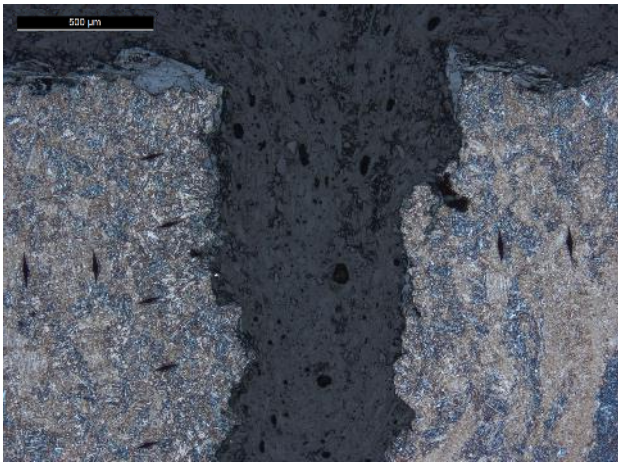

Figure 43. Micrograph at Indication #4 – 50X magnification.

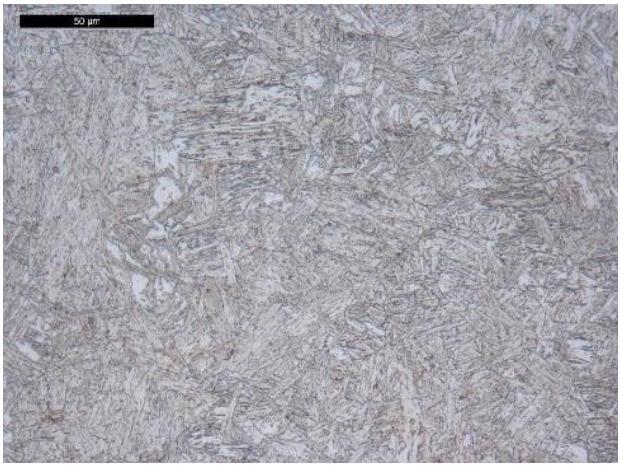

Figure 44. Micrograph at Indication #4 – 500X magnification.

Optical Metallography and Microhardness Testing of Core Samples with Cracks

Optical metallography and microhardness testing were performed on two of the core samples which had been removed from locations SA158W and SA008E due to the detection of crack-like indications with PAUT. The cores were sectioned in the through-thickness direction, perpendicular to the welds, and prepared for metallographic examination. Microhardness readings were taken using a Knoop indenter and a 500-gram load in accordance with ASTM E18–17.

Microhardness readings for Core Sample SA158W started in the weld metal, traversed through the GCHAZ, grain-refined heat-affected zone (GRHAZ), intercritical heat-affected zone (ICHAZ), and terminated in the base metal (Figure 45 and Figure 46). The hardness values are provided in Figure 45 and indicate a weld metal hardness of 365 HV (37.4 HRC), which was slightly harder than the base metal. The GCHAZ was significantly harder than either the weld metal or base metal, with a maximum hardness of 466 HV (46.5 HRC).

Figure 46 and Figure 47 were captured at 50X magnification near the toe of the weld. The crack exhibited an intergranular path through the GCHAZ and GRHAZ, but had not propagated beyond the ICHAZ. The base metal fracture visible in Figure 45 was caused intentionally in order to separate the crack faces for examination.

A microhardness traverse was also performed on the metallographic section taken from Core Sample SA008E, again with readings starting in the weld metal, traversing through the GCHAZ, GRHAZ, ICHAZ, and terminating in the base metal (Figure 48 and Figure 49). The hardness values are provided in Figure 48 and indicate a weld metal hardness of 360 HV (36.9 HRC), which was consistent with the weld metal hardness of SA158W. The maximum hardness recorded in the GCHAZ was 442 HV (44.6 HRC).

The intergranular path of the crack in Core Sample SA008E is clearly visible in Figure 49 and Figure 50. As in SA158W, it progressed through the GCHAZ and GRHAZ before arresting at the ICHAZ. The base metal fracture visible in Figure 48 was caused intentionally in order to separate the crack faces for examination. At 500X magnification, it was clear that the martensite in the GCHAZ had experienced significantly less tempering (Figure 51) than the base metal (Figure 52).

The core sample from weld location SB246E was sectioned across the weld, and Knoop microhardness readings were recorded on each side of the two fusion boundaries; one reading in the weld metal and the other in the GCHAZ. The results are shown in Figure 53.

Cracking was observed in the top weld passes in Core Sample SA168W (Figure 54). Higher magnification of the left-most crack from this location is shown in Figure 55.

Core Sample SA158W	Location	HRC	HV
Crack in GCHAZ and weld metal. Horizontal traverse left to right. 	Weld Metal	37.0	361
	Weld Metal	37.4	365
	GCHAZ	43.0	423
	GCHAZ	44.0	434
	Crack (GCHAZ)	43.1	424
	Crack (GCHAZ)	45.6	454
	GCHAZ	46.5	466
	GRHAZ	46.2	462
	GRHAZ	45.2	449
	GRHAZ	44.3	439
	ICHAZ	33.4	330
	ICHAZ	32.0	319
	Base Metal	31.6	315
	Base Metal	31.6	315

Figure 45. Microhardness traverse for Core Sample SA158W.

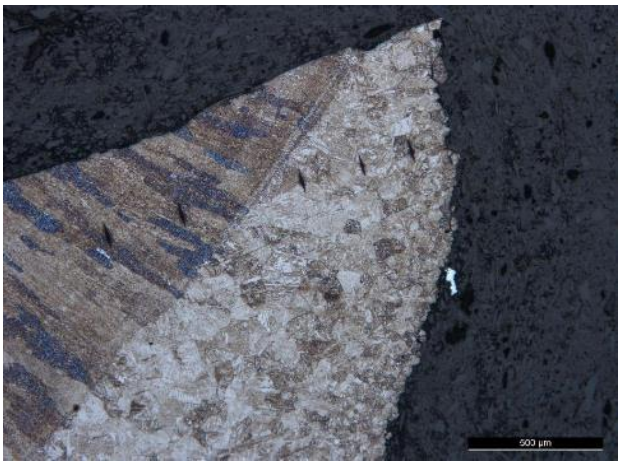

Figure 46. Core Sample SA158W on the weld metal side of the crack – 50X magnification.

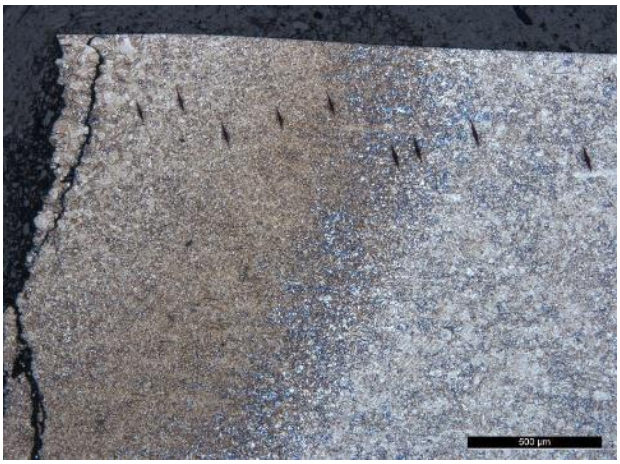

Figure 47. Core Sample SA158W on the base metal side of the crack – 50X magnification.

Core Sample SA008E	Location	HRC	HV
Crack in GCHAZ and weld metal. Horizontal traverse left to right. 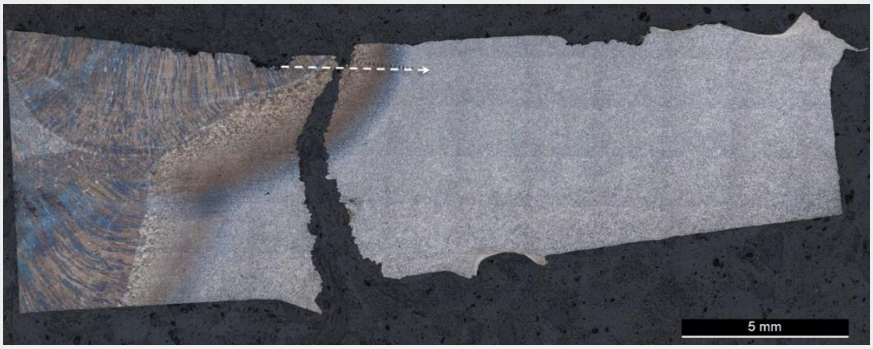	Weld Metal	36.9	360
	Weld Metal	35.0	343
	Crack (GCHAZ)	42.9	422
	GCHAZ	43.9	433
	GCHAZ	44.6	442
	GCHAZ	43.8	432
	GCHAZ	43.0	423
	GRHAZ	42.5	417
	GRHAZ	44.5	440
	GRHAZ	43.3	426
	ICHAZ	39.5	386
	ICHAZ	33.1	327
	ICHAZ	32.8	325
	ICHAZ	31.3	313
	ICHAZ	30.9	310
	Base Metal	28.5	292
	Base Metal	28.1	289
	Base Metal	29.1	296
	Base Metal	30.0	304

Figure 48. Microhardness traverse for Core Sample SA008E.

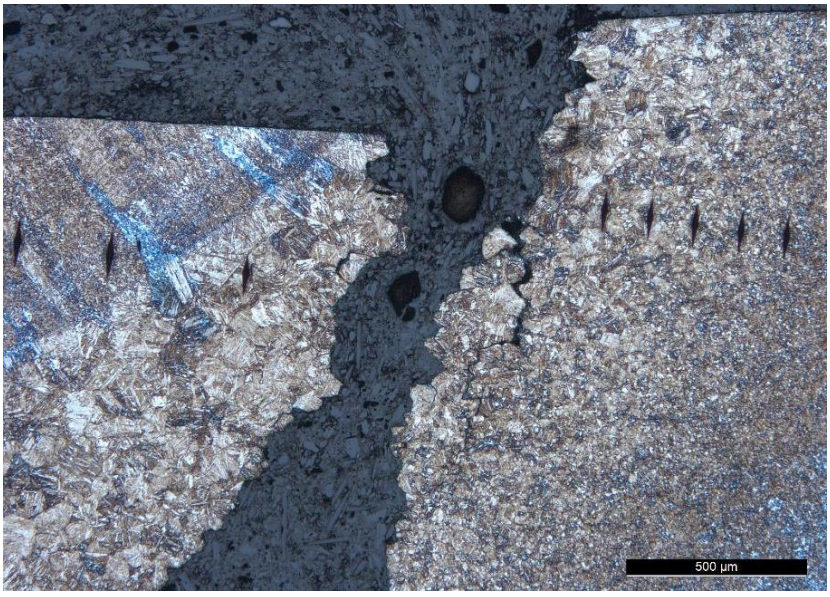

Figure 49. Core Sample SA008E near crack tip. Knoop hardness indentation marks are shown adjacent to the crack – 50X magnification.

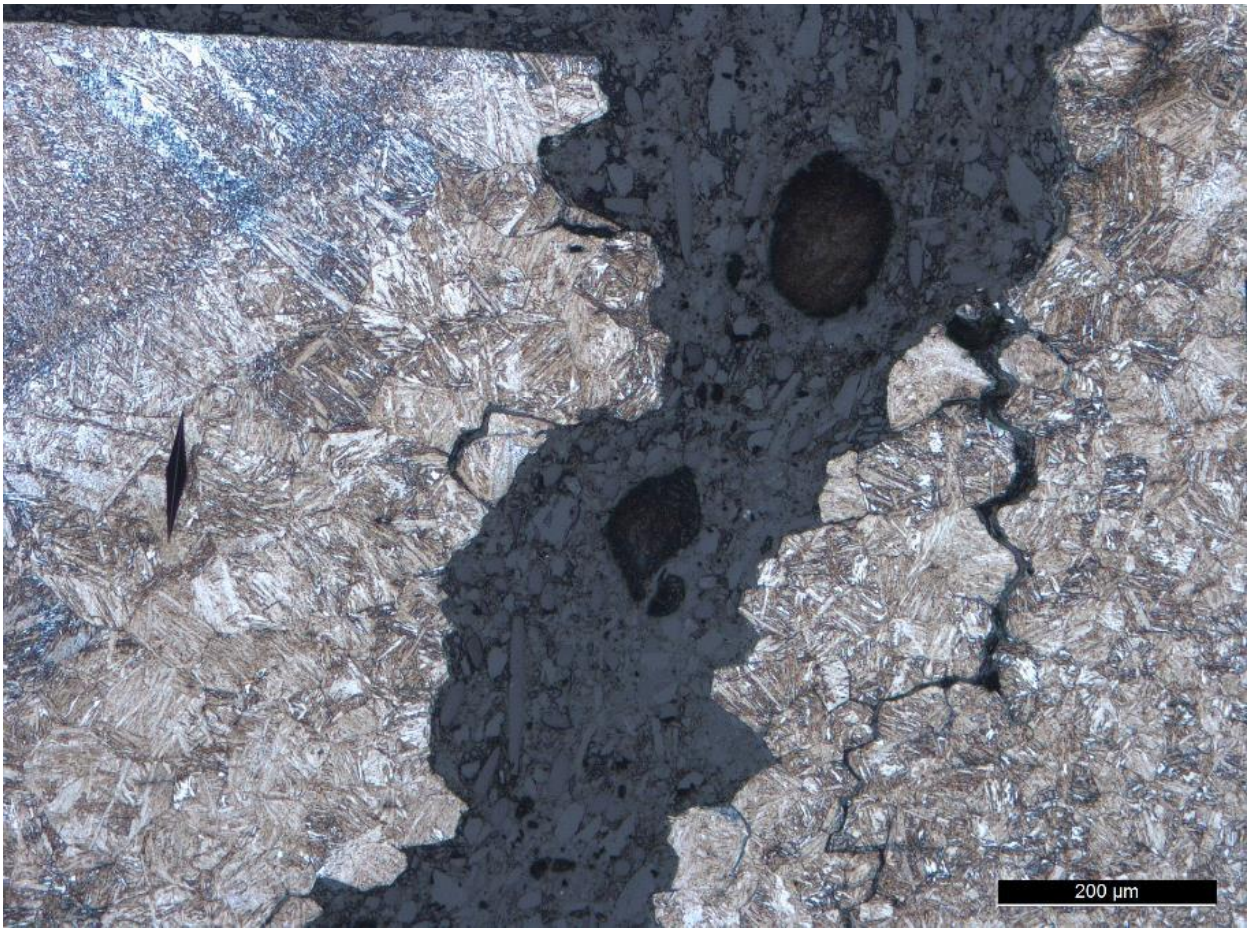

Figure 50. Core Sample SA008E at weld toe. A Knoop hardness indent is shown adjacent to the crack – 100X magnification.

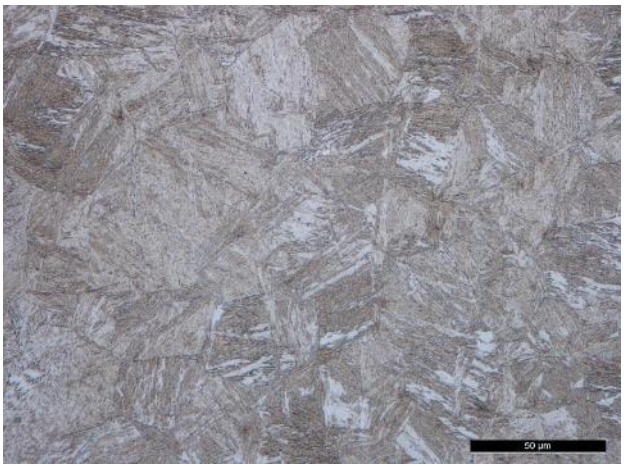

Figure 51. Core Sample SA008E GCHAZ – 500X magnification.

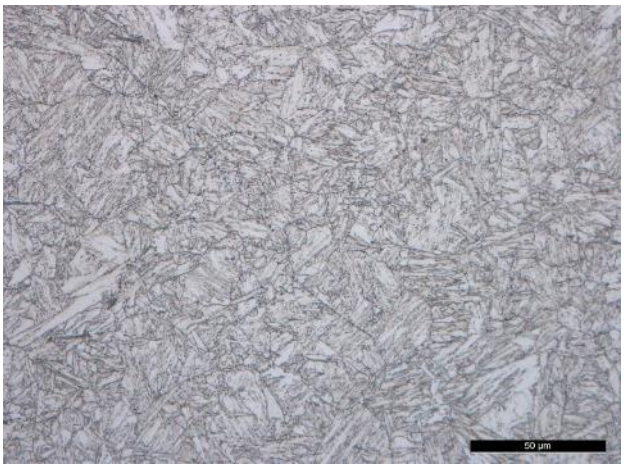

Figure 52. Core Sample SA008E base metal – 500X magnification.

Core Sample SB246E	Location	HRC	HV
Right fusion line (1-3/8-inch plate to weld metal). 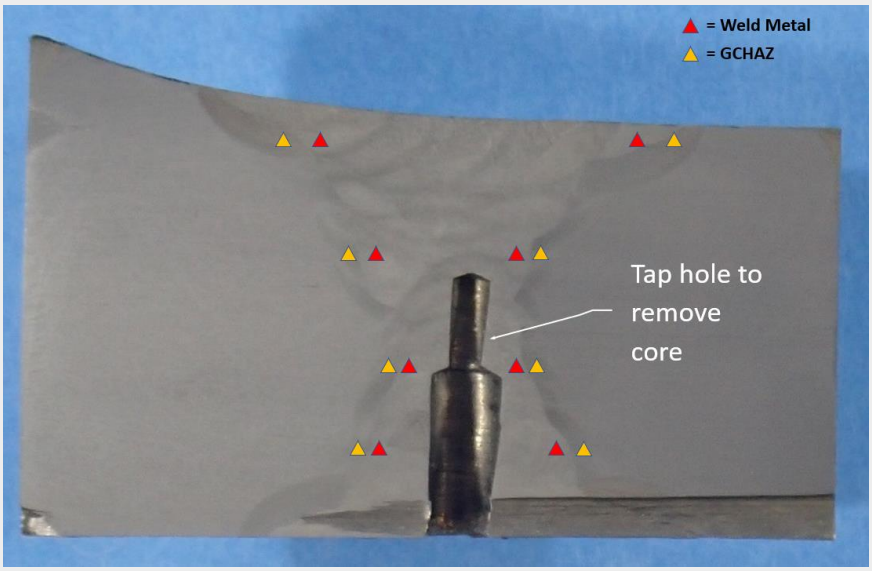	GCHAZ	30.0	304
	Weld Metal	33.0	327
	GCHAZ	34.0	339
	Weld Metal	32.0	316
	GCHAZ	34.0	338
	Weld Metal	30.0	306
	GCHAZ	28.0	286
	Weld Metal	31.0	311
Left fusion line (2-1/4-inch plate to weld metal).	GCHAZ	34.0	333
	Weld Metal	34.0	337
	GCHAZ	33.0	330
	Weld Metal	31.0	311
	GCHAZ	34.0	332
	Weld Metal	32.0	321
	GCHAZ	32.0	321
	Weld Metal	28.0	290

Figure 53. Microhardness traverse for Core Sample SB246E

Figure 54. Cracks in the top weld passes at location SA168W

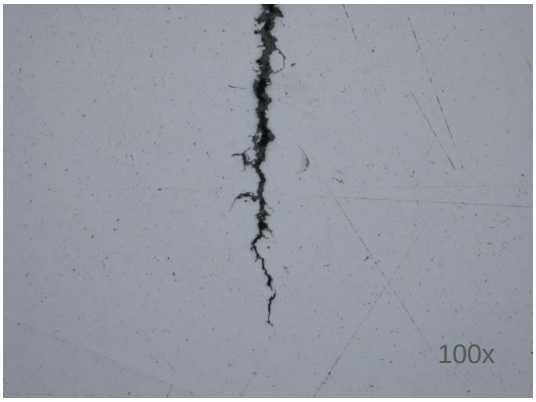

Figure 55. Higher magnification views of a crack observed in SA168W. Unetched.

Chemical Composition Testing

The steel adjacent to the fracture was analyzed by optical emission spectroscopy (OES) in accordance with ASTM E415-17 *Standard Test Method for Analysis of Carbon and Low-Alloy Steel by Spark Atomic Emission Spectroscopy*. The specified and actual values comprising their elemental compositions are listed in Table 2. Four locations were tested, including original weld metal, repair weld metal, and the 2 1/4-inch and 1 3/8-inch thick side plates. Original shop drawings from the fabrication of the bridge indicate that the 2 1/4-inch thick side plates were specified as ASTM A517-69a Grade P, PVQ (Pressure Vessel Quality) steel. The same drawings indicated that the 1 3/8-inch thick plates were specified as ASTM A514-69a Grade M. Three of the individual alloy additions did not conform to specified limits, as indicated by red text in Table 2.

The specified SMAW electrode was not reported to WJE. However, limits on the composition of undiluted weld metal most similar to those of the original and repair weld are included in Table 2 for reference.

Table 2. Material Compositions – ASTM Specifications vs. Test Samples

Element	ASTM 514-69a Gr. M (1 3/8-inch Plate)	ASTM 517-69a Gr. P PVQ (2 1/4-inch Plate)	AWS A5.5-81 E12018-M	1 3/8-inch Side Plate	Original Weld Metal	Repair Weld Metal	2 1/4-inch Side Plate
Carbon	0.10-0.23	0.10-0.23	0.10	0.19	0.07	0.07	0.16
Manganese	0.41-0.74	0.41-0.74	1.30-2.25	0.71	1.55	1.44	0.84
Phosphorus	0.045 max	0.035 max	0.030	0.011	0.006	0.008	0.009
Sulfur	0.05 max	0.040 max	0.030	0.018	0.015	0.014	0.019
Silicon	0.18-0.37	0.18-0.37	0.60	0.34	0.36	0.46	0.22
Copper	(n/s)	(n/s)	(n/s)	0.06	0.39	0.44	0.17
Nickel	1.15-1.55	1.15-1.55	1.75-2.50	1.28	2.38	2.75	0.82
Chromium	(n/s)	0.79-1.26	0.30-1.50	0.17	0.31	0.26	0.57
Molybdenum	0.41-0.64	0.41-0.64	0.30-0.55	0.56	0.50	0.54	0.49
Boron	0.001-0.005	0.001-0.005	(n/s)	0.0063	<0.0005	<0.0005	0.0027
Aluminum	(n/s)	(n/s)	(n/s)	0.08	0.02	<0.005	0.02
Vanadium	(n/s)	(n/s)	0.05	<0.005	0.01	<0.005	0.06
Niobium	(n/s)	(n/s)	(n/s)	<0.005	<0.005	<0.005	<0.005
Titanium	(n/s)	(n/s)	(n/s)	0.02	<0.005	<0.005	<0.005
Cobalt	(n/s)	(n/s)	(n/s)	0.06	0.03	—	0.02

Mechanical Testing

Tensile Properties

Samples from the fractured plates were prepared and tension-tested in accordance with ASTM A370–20 *Standard Test Methods and Definitions for Mechanical Testing of Steel Products* and ASTM E8-21 *Standard Test Methods for Tension Testing of Metallic Materials*. Two tensile tests were performed for each material. Each was machined from material at the mid-thickness for plates under 1 1/2-inches and at the quarter thickness for the 2 1/4-inch plate. The test results and the sample geometries used for the testing are shown below in Table 3 and Table 4. . All of the test samples for the A514 material met the requirements for A514-69a Gr M steel. The yield strength and tensile strength results from the tests for the 2 1/4-inch steel side plate material fell below the minimum material specifications for the A517-69a Gr P (PVQ) in both tests. The low values are highlighted red in Table 4. The sample geometry varied somewhat from that prescribed by the original specification for some samples. For the 2 1/4-inch side plate material, the 1/2-inch diameter sample size was allowed by the original plate specification.

Table 3. Specified and Actual Tensile Properties for ASTM A514-69a Gr. M Steel

Property	ASTM A514-69a Gr. M (From Table 2 in A514)	Top Cover Plate (1/2-inch)		Bottom Cover Plate (1/2-inch)		Side Plate (1 3/8-inch)	
Sample Geometry		Rectangular		Round		Round	
Sample Dimensions		0.525" x 0.500"		0.250"		0.250"	
Test #		1	2	1	2	1	2
Yield Strength (ksi)	100 min	115.2	116.0	114.5	115.2	110.4	110.7
Tensile Strength (ksi)	115-135	123.5	123.7	123.7	123.9	120.6	120.7
Elongation (%)	18 min	24.5	23.0	20.0	20.0	19.0	18.5
Reduction of Area (%)	50 min	48.2	52.6	67.4	67.0	52.8	52.8

Table 4. Specified and Actual Tensile Properties for ASTM A517-69a Gr. P (PVQ) Steel

Property	ASTM A517-69a Gr. P (From Table 2 in A517)	Side Plate (2 1/4-inch)	
Sample Geometry		Round	
Sample Dimensions		0.500"	
Test #		1	2
Yield Strength (ksi)	100 min	96.8	97.0
Tensile Strength (ksi)	115-135	112.0	111.8
Elongation (%)	16 min	26.5	25.0
Reduction of Area (%)[1]	45 min	67.2	67.3
Note 1: For A 370 1/2" rounds			

Charpy Impact Testing

Plate samples were sent for Charpy V-Notch (CVN) impact testing. The tests were conducted in accordance with the ASTM A673-17 *Standard Specification for Sampling Procedure for Impact Testing of Structural Steel.* The test temperatures were set to –20 deg. F, 10 deg. F, 40 deg. F, and 70 deg. F to develop the upper and lower shelf toughness behavior of the material. The results of the base material tests for the cover plates and 1 3/8-inch side plate are shown in Table 5a and b. The initial test results were invalid for the 2 1/4-inch plate, thus additional 2 1/4-inch plate material was sent to another laboratory for testing. Those test results are presented in Table 5c. An upper temperature value of 100 deg. F was used for these tests. The CVN results for the base materials are plotted in Figure 56 through Figure 58. The average for each test was greater than 15 ft-lbs.

The weld and HAZ CVN samples were obtained from the 2 1/4-inch plate side of the weld. There was insufficient material available to obtain CVNs from the 1 3/8-inch side of the weld. To maximize the number of tests from the available weld and HAZ materials, a combination of full-size and half-size CVNs were machined. The half-size CVN test results have not been adjusted to represent full-size specimens. Results for the weld and HAZ CVN tests are presented in Table 5d and e. Figure 59 and Figure 60 are plots of these results. The variability in the test results for the HAZ specimens shown in Figure 60 suggests notch placement inconsistencies within the HAZ.

Table 5. Charpy V-notch results

a. Material: ASTM A514-69a Grade M; No CVN requirement.								
Charpy V-notch	**Top Cover PL (1/2-inch) (ft-lbs.)**				**Bot. Cover PL (1/2-inch) (ft-lbs.)**			
Temperature (Deg. F)	**1**	**2**	**3**	**Avg**	**1**	**2**	**3**	**Avg**
-20	19	16	17	**17.3**	21	32	26	**26.3**
10	22	30	23	**25.0**	29	37	32	**32.7**
40	43	38	37	**39.3**	60	42	55	**52.3**
70	42	43	41	**42.0**	60	58	59	**59.0**
b. Material: ASTM A514-69a Grade M. No CVN requirement.								
Charpy V-notch	**1 3/8-inch Side Pl (1/4T) (ft-lbs.)**				**1 3/8-inch Side Pl (1/2T) (ft-lbs.)**			
Temperature (Deg. F)	**1**	**2**	**3**	**Avg**	**1**	**2**	**3**	**Avg**
-20	20	21	20	**20.3**	17	19	17	**17.1**
10	19	22	23	**21.3**	19	22	22	**21.0**
40	27	24	27	**26.0**	28	27	26	**27.0**
70	28	28	27	**27.7**	29	29	30	**29.3**
c. Material: ASTM A517-69a Grade P PVQ BAE (2). CVN required. This value is agreed upon by the manufacturer and the purchaser, but shall not be conducted greater than 32 °F.								
Charpy V-notch	**2 1/4-inch Side Pl (1/4T) (ft-lbs.)**							
Temperature (Deg. F)	**1**	**2**	**3**	**Avg**				
-20	40	42.5	36	**39.5**	--	--	--	**--**
40	58	62	56.5	**58.8**	--	--	--	**--**
100	57	53.5	54	**54.8**	--	--	--	**--**
d. Material: Weld Metal and HAZ 1/2-Size CVN (Actual values without adjustment to full-size)								
Charpy V-notch	**Weld Metal 10x5x55 mm (ft-lbs.)**				**HAZ 10x5x55 mm (ft-lbs.)**			
Temperature (Deg. F)	**1**	**2**	**3**	**Avg**	**1**	**2**	**3**	**Avg**
-20	20	20	17	**19.0**	44	42	37	**41.0**
10	18	18	17	**17.7**	21	23	28	**24.0**
40	19	16	19	**18.0**	43	29	23	**31.7**
70	19	19	19	**19.0**	38	22	52	**37.3**
e. Material: Weld Metal and HAZ Full-Size CVN								
Charpy V-notch	**Weld Metal 10x10x55 mm (ft-lbs.)**				**HAZ 10x10x55 mm (ft-lbs.)**			
Temperature (Deg. F)	**1**	**2**	**3**	**Avg**	**1**	**2**	**3**	**Avg**
-20	-	-	-	**-**	-	-	-	**-**
10	31	30	34	**31.7**	45	45	49	**46.3**
40	33	34	-	**33.5**	47	39	-	**43.0**
70	-	-	-	**-**	-	-	-	**-**

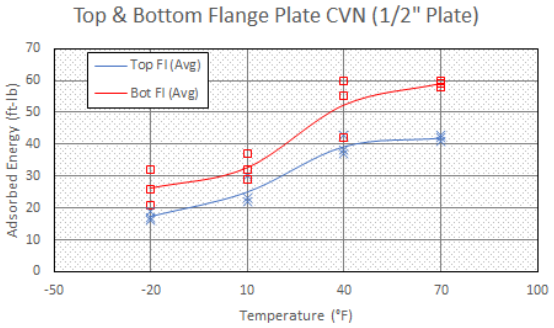

Figure 56. CVN test results for the top and bottom cover plate material.

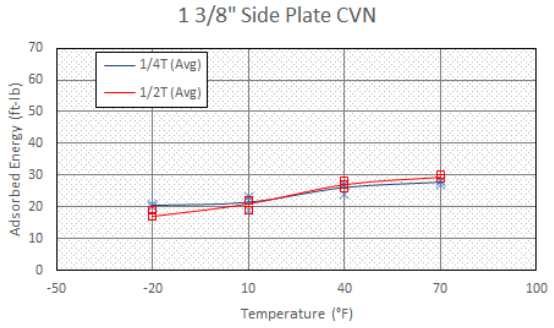

Figure 57. CVN test results for the 1 3/8-inch side plate material.

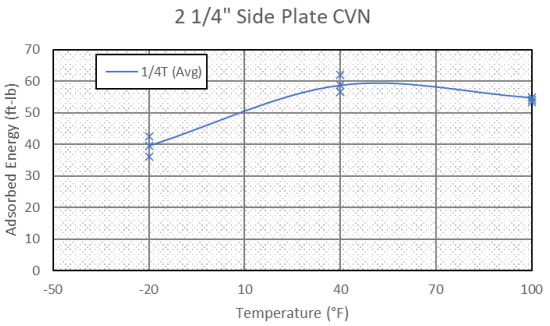

Figure 58. CVN test results for the 2 1/4-inch side plate material.

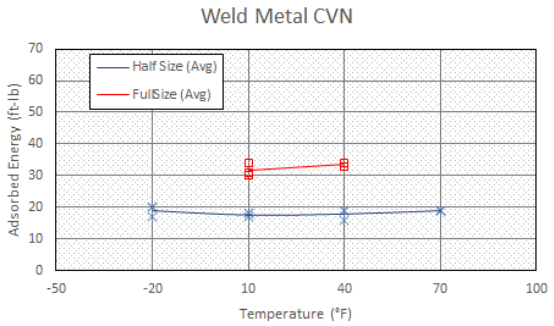

Figure 59. CVN test results for the weld metal material.

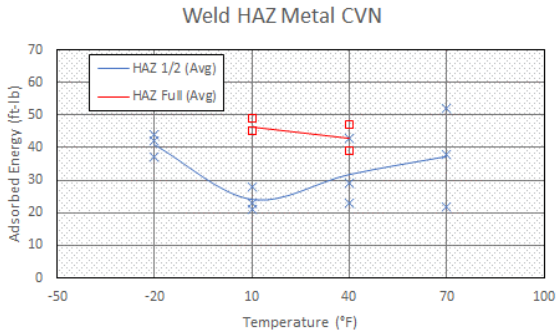

Figure 60. CVN test results for the material in the weld HAZ.

DISCUSSION

The chemical and physical properties of the materials tested as a portion of this study were found to be in general conformance with the original project requirements. Nominal variations from specification were identified for some of the alloying components of the steel base metals. The 2 1/4-inch thick side plate

material was found to have tested about 3 percent low with regard to yield and tensile strength. These plate properties were not judged to be contributory to the fracture study.

The poor conditions of the primary and secondary preexisting crack regions when compared to the fracture surfaces indicates those surfaces were exposed the longest to the corroding effects of moisture and were the oldest cracks along the fracture surface. Moreover, the primary preexisting crack region was noticeably more corroded than the secondary. Despite the pervasive loss of fracture face microtopography caused by post-failure corrosion, the macrotopography, supported by metallographic examination, provided sufficient basis for determining the origin of the fractures and the likely failure sequence at the NB222W weld region.

In addition, the investigation was aided by the examination of other cracks identified within the NB222W fractured weld and core samples removed from welds in other side plate thickness transitions from the bridge that were identified during a recent PAUT inspection of all similar bridge joints performed by others. Based on these studies, some discussion on the susceptibility of the tie girder to another fracture was made.

Fracture Origin and Propagation

The regions designated in this report as Primary Preexisting Crack and Secondary Preexisting Crack were apparently weld repairs that had been performed on the interior face of the groove welds during fabrication. The two weld repairs resulted in what became essentially contiguous regions of cracking that extended through the entire depth and length of each weld repair, indicated in color-coded Figure 61 as yellow (Primary) and green (Secondary). No fabrication records discussing the weld repair locations, extent, or procedures were available for review.

In high-strength, quenched and tempered alloy steels such as A514 Grade M and A517 Grade P, welded with strength-matching filler metal, GCHAZ and weld metal hydrogen cracking are an ever-present risk during fabrication. The intrinsically high-restraint nature of repair welds makes them particularly susceptible. Today, strict adherence to code-specified hydrogen control measures, including electrode maintenance and base metal preheating, are just part of a fabricator's fracture control plan which also includes post-weld inspections and nondestructive testing. However, during the era when these tie girders were fabricated, such measures were not fully understood or practiced. As a result, several interstate tied arch structures including the I-24 Bridge between Metropolis, Illinois and Paducah, Kentucky[2] and the I-79 bridge in Neville Island, Pennsylvania[3] experienced weld cracking in the tie girders in the late 1970s and early 1980s. The issues with these other tied arch structures may have been the impetus behind the 1982 weld inspections of the I-40 Bridge. It was not until the mid-to-late 1980s that implementation of fracture control plans for fracture critical members in bridges was common.

The locations and orientations of the large cracks observed within the GCHAZs and weld metal of the multi-pass repair welds indicated tensile residual rather than applied stresses as their primary drivers,

[2] Fisher, J.W. and Yuceoglu, U.; A Survey of Localized Cracking in Steel Bridges, Fritz Engineering Laboratory, Lehigh University, Bethlehem, PA, Interim Report Sept. 1978 to June 1981.

[3] Fisher, J.W., Pense, A.W., Menzemer, C.C., and Kauffman, E.J., Final Report on I79 Tied Arch Cracking – Neville Island Bridge, FHWA/PA-84-016, Fritz Engineering Laboratory, Lehigh University, Bethlehem, PA, December 1984

suggesting that the observed cracking had preceded the application of any service loads. A well-known susceptibility to hydrogen cracking, along with corroborating observations of fracture surface macro- and microtopography, led to the conclusion that hydrogen cracking created these cracks. By the same token, the magnitudes of the applied service loads that initiated subsequent fracture events were not limited by the fracture toughness of >345 HV (>35 HRC) HAZ material, which had already been cracked by residual stresses and hydrogen. Rather, they were determined by the fracture toughness of the unaffected base metal that lay along the extremities of the hydrogen-cracked regions. Also, the propagation and arrest behavior of the same fracture events were influenced by base metal rather than weld metal or HAZ properties.

It is known that the reduced hydrogen diffusion rates caused by the alloy content of the A514/A517 grades may in rare cases extend the incremental growth of hydrogen cracks to times exceeding 100 hours.[4] Suggesting this possibility in the present case was the elevated nickel content of the weld metal, particularly in the repair weld associated with the Primary Preexisting Crack (see Table 2). However, the earliest UT-detectable cracks within the repair welds most likely occurred within hours of repair weld completion[5] and were not detected by any post-weld repair fabrication quality control testing. Moreover, it appears that despite the ability to find small defects as demonstrated by the flaw shown in Figure 11, these two unusually large defects went undetected in the 1982 UT inspection.

Careful examination of the entire length and width of the cracks and unstable fracture associated with the NB222W weld produced no evidence of fatigue crack growth. Therefore, these two large defects (green and yellow in Figure 61) remained unchanged for a number of years. At some point, the tip of the hydrogen-cracked region positioned closest to the bottom cover plate became unstable. A fracture then ran in all possible directions from the Primary Preexisting Crack, to the extent indicated as blue in Figure 61, and then was arrested in the secondary preexisting hydrogen-cracked region (green). At this point, the crack appears not to have been through-thickness and thus, not visibly observable on the exterior face of the side plate. At a later time, the upper tip of the Secondary Preexisting Crack (green) in turn became unstable, ran upward for approximately 8 inches (orange in Figure 61 and Figure 62) and rearrested in the 1 3/8-inch plate material. It appears that the fracture also caused the remaining portions of the side plate (orange) below the Secondary Preexisting Crack to experience tensile-shear rupture, including a portion of the bottom cover plate which experienced tensile-shear fracture. This second stage of crack propagation is likely what was visible in the 2016 photo and what is seen in the 2019 drone video.

The instabilities of the three fractures and subsequent arrests did not occur because of reduced material toughness due to reduced temperatures as the cracks were able to arrest themselves. Meaning, had the tie girder materials experienced a reduction in fracture toughness due to low temperatures, there would have been only one fracture, likely extending through the entire tie cross section. A review of the temperature records in Memphis between 2015 and 2019 found no unusually cold temperatures (<5 deg. F) that may have affected the notch toughness of the materials and caused the crack instability. The coldest temperatures experienced by the bridge were shortly after the 1982 UT inspections when

[4] Pargeter, R., "Evaluation of Necessary Delay before Inspection for Hydrogen Cracks," *Welding Journal*, 82(11), Nov. 2003, pp. 321s–329s.

[5] Ibid.

temperatures below 0 deg. F were recorded multiple times. But as observed by the recent instrumentation measurements, the load in the tie girders increases with decreasing temperatures. Further, the degree to which the friction pendulum bridge bearings are able to act as a fuse for this loading mechanism appears to require additional study based on recent measured performance. Thus, it is likely the existing weld repair cracks became unstable as a result of a unique combination of low temperatures increasing tie girder stress and high live loads to which the bridge had not been previously subjected.

The photographic documentation indicates that at some point after 2019, the crack tip of the arrested second unstable fracture (orange) became unstable, ran upward over the remaining 6 1/2 inches of the side plate's height and continued into the top plate (magenta in Figure 62). It then turned and ran longitudinally along the fillet welded connection between the tie girder top cover plate and the inboard side plate for some distance before it was found in May 2021.

There was no significant yielding of the side plate or the top plate. The bottom plate showed some yielding. The uncracked tie girder cross section had about 40 ksi of dead load stress. The maximum stress as the crack continued to propagate never exceeded the yield strength of the material in the remaining intact section. Of the approximately 51.5 square inches of material that remained, a stress in the material of about 88 ksi plus live load and the effects of residual stresses and eccentricity was generated, still likely less than the minimum-tested 110 ksi yield strength of the plates.

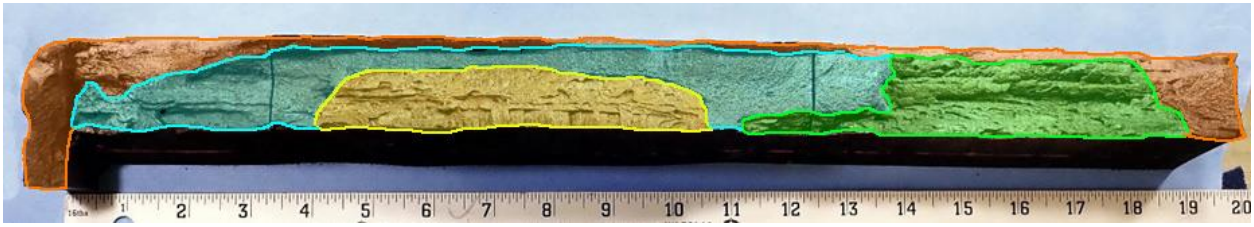

Figure 61. Lower portion of fracture, color-coded to indicate failure sequence.

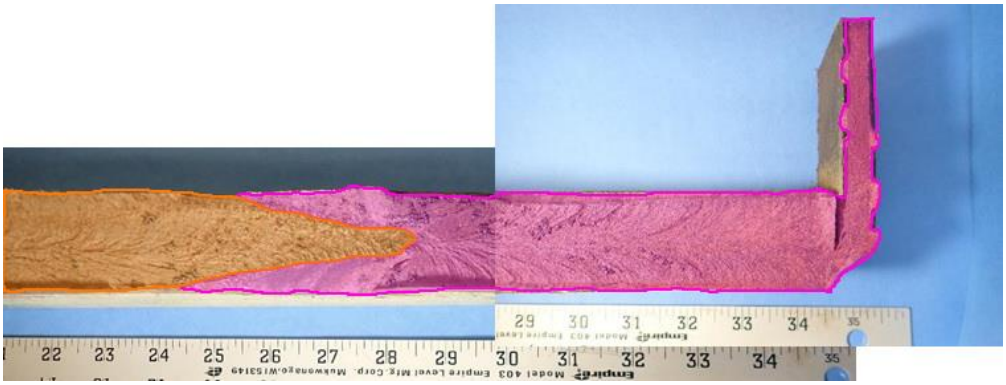

Figure 62. Upper portion of fracture, color-coded to indicate failure sequence.

Fracture Study

The presence of hydrogen cracks in welds was not limited to just the weld repairs. Various weld-related, surface-breaking crack indications were detected and subsequently diagnosed as shallow hydrogen cracks

in the same weld that fractured as well as in other tie girder side plate welded thickness transitions. Visual, SEM, and metallographic examinations of these smaller cracks also revealed no evidence of fatigue crack growth or any other service-related progressive cracking mechanism. Moreover, the depths of these hydrogen cracks has been limited to that of a single weld pass by their propagation from highly-susceptible GCHAZ microstructures into less-susceptible, grain-refined HAZ microstructures. Given their continued stasis throughout nearly five decades of service, these observations indicate further stable crack growth to be highly unlikely.

An analysis of K_{1c} data for construction steels by Barsom[6] has demonstrated that for steel having yield strengths between 36 and 130 ksi, they provide a temperature shift between static and impact fracture toughness by the relationship in Equation 1.

$$T_s = 215 - 1.5\sigma_{ys} \qquad 1$$

The Charpy V-notch impact test is the most widely used test for steel quality control and Barsom developed a correlation between CVN test results and the impact plane-strain fracture toughness, K_{1d}, by the relationship in Equation 2.

$$K_{1d} = [5(CVN)E]^{0.5} \qquad \text{(ksi}\sqrt{\text{in.}}\text{, ft-lbs, psi)} \qquad 2$$

The results of the fracture study are presented in Table 6 which indicates that at the subject weld joint the 1 3/8-inch side plate has the least resistance to crack extension while the 2 1/4-inch side plate has the highest resistance to unstable crack growth.

CVN results obtained from what had been intended to be HAZ material suggested a fracture toughness of 80.3 ksi√in. with a temperature shift of 50 deg. F when a 110 ksi yield strength is used. However, the microhardness values suggest the HAZ had a much higher yield strength, and therefore, the above fracture toughness equations may not be applicable. Furthermore, examination of CVN specimen fracture surfaces indicated that only 20 to 30 percent of the notch length had been interacting with HAZ material. Therefore, the CVN values plotted in Figure 60 are not indicative of the predicted fracture toughness and for reasons given earlier are of minimal significance to the subsequent in-service fracture events demonstrated at the subject joint. However, it is possible that further in-depth study of the HAZ at representative in-service welded joints on this bridge could provide additional information with regard to fracture susceptibility.

At first glance it might seem contradictory that the plate material exhibiting the highest CVN impact resistance and estimated fracture toughness was found to have an unusually coarse grain size. In a martensitic microstructure, grain size actually refers to the prior (pre-quench) austenite grain (PAG) size. In the absence of a PAG boundary embrittling mechanism such as tempered martensite embrittlement (TME), the toughness of tempered martensite does not directly correlate with PAG size. Although a coarse PAG does increase the risk of TME, there was no evidence of intergranular fracture in the base metal CVN test specimens. In the present case, therefore, TME was not a factor, and toughness would have been determined predominantly by the degree of tempering and the martensite lath morphology. The

[6] Barsom, J. and Rolfe, S., "Correlations Between KIc and Charpy V-Notch Test Results in the Transition-Temperature Range," in *Impact Testing of Metals*, ed. D. Driscoll (West Conshohocken, PA: ASTM International, 1970), 281-302.

observed lower yield strength of the 2 1/4-inch plate material was consistent with greater tempering, which is positively and strongly correlated with toughness. Moreover, in terms of quench response in the production of quenched and tempered steel plate, coarser-grained austenite at the moment of quenching has greater hardenability than finer-grained austenite of the same composition. As a result, 2 1/4-inch plate with coarse PAGs is more likely than the same plate with fine PAGs to exhibit a uniformly martensitic microstructure, particularly near mid-thickness. Once tempering has been performed, and absent TME, a uniformly martensitic steel should exhibit greater toughness than one containing a small microstructural fraction of bainite and/or ferrite.

Table 6. Fracture Study Results

Element	CVN @ 40 °F (ft-lbs.)	Yield Stress, σ_Y (ksi)	Temperature Shift (°F)	Fracture Toughness (ksi√in.)
1/2-in. Top Plate	39.3	115.6	42	76.8
1/2-in. Bottom Plate	52.3	114.9	41	88.6
1 3/8-in. Side Plate	27.0	110.6	49	63.6
2 1/4-in. Side Plate	58.8	96.9	70	93.9
Weld Metal	33.5	110	50	70.9
HAZ[1]	43.0	110	50	80.3

Note 1: See discussion above for further information.

Future Bridge Inspections

Work under this study has confirmed that PAUT indications from other similar welded thickness transitions throughout the bridge tie girders were consistent with shallow hydrogen cracks present on the inside surface of the tie girder box members. Mitigation strategies for these findings have been or are in process of execution by others. No large defects such as the Primary Preexisting Crack or the Secondary Preexisting Crack were identified through the recent PAUT inspection. However, it is a clear possibility that other small (short length and/or shallow) cracks exist in the tie girder welded thickness transitions. Similar shallow hydrogen cracks identified through this study were found to typically initiate in GCHAZ regions with high hardness characteristics and low resistance to crack propagation, but terminated in GRHAZ or other surrounding material with higher fracture toughness and lower susceptibility to hydrogen cracking. These cracks were formed soon after fabrication and prior to application of service loads.

The properties of the constituent fractured joint parts (e.g. base metals, HAZ, weld metal) suggest that additional hydrogen cracking is unlikely for the environmental conditions to which these joints are subjected in service and that advancement of these cracks has not occurred through fatigue. However, this study identified an unknown combination of tie girder loading which likely included thermal effects in combination with live loads that advanced the Primary Preexisting Crack and Secondary Preexisting Crack at different times. It is therefore possible that this unknown combination of loading could advance another small existing hydrogen crack in the future.

Given the service history of the fracture under study, it is unlikely that advancement of a small existing hydrogen crack would immediately lead to brittle fracture of the entire tie girder cross section. However, it would be prudent to continue arms-length inspection of the tie girders at regular intervals, as required by the National Bridge Inspection Standards. In addition, non-destructive testing (UT or PAUT) should be

performed periodically (~10 year interval) to interrogate the volumetric integrity of these tie girder thickness transition regions, and specifically look for any crack advancement from the interior surface of the welded joints.

CONCLUSIONS

- Metallographic examination of the fracture surfaces identified two weld repairs from fabrication that were much wider and contained weld metal deposit sequencing that differed from other side plate thickness transition welds in the bridge.
- The weld repairs caused two large hydrogen cracks as a result of the inherent restraint, improper preheat and/or use of contaminated welding electrodes commonly associated with weld repairs performed without a fracture control plan.
- The large hydrogen cracks escaped detection during fabrication and later UT inspection and once surface breaking, were not visually detected for at least three years if not more than five years.
- The tie girder fracture at the NB222W side plate thickness transition complete joint penetration weld occurred in three stages.
  - The first stage of fracture (blue in Figure 61) initiated at a preexisting repair weld hydrogen crack near the bottom of the outboard side plate (Plate 2). Travelling nearly through the plate thickness, this fracture travelled down to, but not into, the bottom cover plate (Plate 3) before it arrested. It also travelled upward and arrested at the second preexisting repair weld hydrogen crack.
  - The second stage of fracture (orange in Figure 61 and Figure 62) initiated at the upper preexisting repair weld hydrogen crack near mid-height of the side plate (Plate 2) and travelled upward where it arrested in base metal. The fracture also appears to have fractured the remaining lower side plate material and extended into the bottom cover plate (Plate 3) where it arrested. This crack should have been visible on the exterior face of the tie girder.
  - The third stage of fracture (magenta in Figure 62) initiated at the previous fracture arrest location in the base metal. This fracture travelled upward and through the top cover plate (Plate 1), where displacement between the two tie girder segments unzipped the longitudinal length of fillet weld between the top cover plate and inboard side plate (Plate 4). The fracture also appears to have extended the existing crack in the bottom cover plate a small amount.
- The initial instability of the repair weld hydrogen cracks as well as subsequent fracture extensions were likely the unique combination of increased tie girder stresses due to low temperatures and the effects of live loads.
- Careful study of the NB222W fracture surfaces and the core sample cracks indicated no evidence of fatigue crack growth.
- Other hydrogen cracks were identified on the interior tie girder surface at similar thickness transitions throughout the bridge. These hydrogen cracks were comparatively shallow (<3/16 in.), and those observed cracks tended to travel as intergranular cracks through the GCHAZ until they arrested in material with lower hardness and greater toughness and hydrogen tolerance.
- Charpy V-Notch (CVN) testing of the NB222W parent base metals, weld metal, and HAZ indicated reasonably good toughness values. Based on this information, a lower bound fracture toughness

estimate of 63.6 ksi√in. for the 1 3/8-inch side plate was calculated. Significant variation in CVN test results through the thickness of the 1 3/8-inch side plate was not observed.

- The chemical and physical properties of the materials tested as a portion of this study were not judged to be contributory to the fracture under study. Further, the nonconforming grain size observed in the 2 1/4-inch side plate appears not to have contributed to the fracture and is not an indication, for this plate, that fracture toughness is a concern.
- Given the 48-year service life of this structure, the fact that the subject fracture occurred in three separate phases over several years, the recent inspection efforts to identify welding defects at the tie girder thickness transition welds, and no evidence of observed fatigue crack growth during this study, it is highly unlikely that an additional major fracture of a similar tie girder thickness transition weld will occur.
- It is prudent to continue regular biannual arms-length fracture critical inspections with ultrasonic testing performed on a periodic (≈10 years) basis.

ACKNOWLEDGEMENTS

WJE would like to acknowledge the assistance of Kiewit Construction personnel in removing the fractured tie plates as well as the ArDOT Snooper crew who provided access and assistance during removal of the core samples.

A Quality Assurance review of this investigation was provided by Dr. John W. Fisher, Lehigh University and Dr. Eric Kauffmann. We thank them for their consultation and expertise.